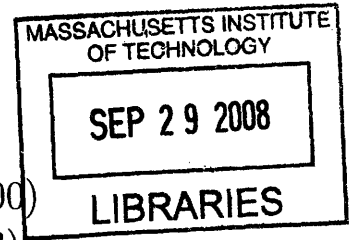


# A Sphere Settling in a Stratified Fluid at Small Reynolds Number

by

King Yeung Yick

B.Eng., The Chinese University of Hong Kong (2000)  
S.M., Massachusetts Institute of Technology (2003)



Submitted to the Department of Mathematics  
in partial fulfillment of the requirements for the degree of

DOCTOR OF PHILOSOPHY

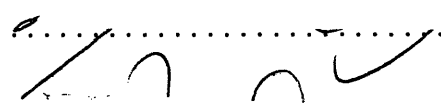
at the

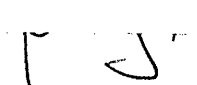
MASSACHUSETTS INSTITUTE OF TECHNOLOGY

September 2008


©King Yeung Yick, 2008. All rights reserved.

The author hereby grants MIT permission to reproduce and to distribute publicly paper and electronic copies of this thesis document in whole or in part in any medium now known or hereafter created.

Author .....  
  
Department of Mathematics  
July 28, 2008

Certified by .....  
  
Roman Stocker  
Assistant Professor of Civil and Environmental Engineering  
Thesis Supervisor

Accepted by .....  
Alar Toomre  
Chairman, Applied Mathematics Committee

Accepted by .....  
  
David Jerison  
Chairman, Department Committee on Graduate Students



# A Sphere Settling in a Stratified Fluid at Small Reynolds Number

by

King Yeung Yick

Submitted to the Department of Mathematics  
on July 28, 2008, in partial fulfillment of the  
requirements for the degree of  
DOCTOR OF PHILOSOPHY

## Abstract

We present a combined theoretical, experimental and numerical investigation of a sphere settling in a linearly stratified fluid at low Reynolds number ( $0.01 \leq Re \leq 2.1$ ). We developed the microscale Synthetic Schlieren technique to study the wake of a microscale sphere settling through a density stratification. A video-microscope was used to magnify and image apparent displacements of a micron-sized random-dot pattern. Due to the nature of the wake, density gradient perturbations in the horizontal direction greatly exceed those in the vertical, requiring modification of a previously developed axisymmetric technique. We demonstrated that Schlieren could be extended to microscale ( $100 \mu m$ ) and obtained the first quantitative measurement of the density field in the wake of a sphere settling in a stratified fluid. As stratification breaks directional symmetry, the direction of motion strongly influences the dynamics, unlike in the homogeneous case. Previous work primarily focused on particles moving parallel to isopycnals. Here we investigate motion perpendicular to isopycnals. As the sphere settles, the particle draws lighter fluid downwards, generating buoyancy forces: this results in a long density wake, extending many particle diameters downstream. Using time-lapse photography, the drag on the sphere was measured and we have obtained the first experimental quantification of the added drag on a sphere due to stratification. We found that stratification increases the hydrodynamic drag, and that the added drag coefficient scales with the Richardson number  $Ri = a^3 N^2 / (\nu U)$  as  $Ri^{1/2}$ , where  $a$  is the particle radius,  $U$  its speed,  $\nu$  the kinematic fluid viscosity and  $N$  the buoyancy frequency. These observations are confirmed by numerical simulations, and are in contrast with earlier results for higher  $Re$ . By analyzing the numerical velocity, pressure, density and vorticity fields around the sphere, we found that the pressure and viscous drags both increased with stratification. Combining these analyses with the investigations on isopycnal perturbations around the sphere and the buoyancy force in the wake, we conclude that the bulk of the wake does not contribute to the drag. Based on the experimental and numerical results, we derived a scaling argument which suggests that the added drag results from the buoyancy of the fluid in a small region of width  $(\nu/N)^{1/2}$  around the sphere. Here the physical

mechanism responsible for the added drag in a stratified fluid at low  $Re$  is drastically different from mechanisms proposed at higher  $Re$ . The observed increase in drag could enhance retention time of particles at density interfaces as the parameter regime studied here applies to small particles in the ocean and affects the ecology of marine microorganisms by influencing particle-organism interactions.

Thesis Supervisor: Roman Stocker

Title: Assistant Professor of Civil and Environmental Engineering



# Acknowledgments

When I was watching Academy Awards on television, I always wondered why those who won an Oscar had so many people to thank. Now I understand better. I would not have been able to complete this thesis without the aid and support of countless people over all these years. I will forever be grateful to them for the completion of this thesis.

My first, and most earnest, acknowledgment must go to my advisor, Prof. Roman Stocker. He contributed tremendously to my development, both scientifically and personally. He always challenged me to do my best, and never shied away from telling me when I was not doing my best. Words alone can't express how thankful I am.

I also owe a huge debt of gratitude to the members of my thesis committee. Prof. Thomas Peacock co-authored my two papers and it is only through collaboration with him that I can finish this thesis. He was also the first person who taught me scaling analysis years ago, a technique that proved useful in this research. I took my first fluid mechanics course with Prof. John Bush, and I would like to thank him for our discussions on this project, which provided me with valuable physical insights. I also enjoyed the discussions with Prof. Rodolfo Rosales. Our discussions on numerical simulations and partial differential equations gave me better insight on these topics than all the related courses I took before.

Thanks must also go to Dr. Carlos Torres, who kindly performed the numerical simulations of this study. I would also like to thank Prof. Bruce Sutherland and Prof. Stuart Dalziel for thorough discourse on Synthetic Schlieren, in particular the former for providing a version of the axisymmetric code for validation and the latter for access to DigiFlow. I am equally grateful for the helpful discussions with Prof. Paul Linden and Prof. Francois Blanchette. I like to express my gratitude to Tanvir

Ahmed for help in generating the mask used in Schlieren and Zheng Gong for assistance with experiments in time-lapse photography.

I am tempted to individually thank all of my friends, from my childhood until graduate school, without whom my life would have been much less colorful. However, because the list might be too long and by fear of leaving someone out, I will simply say thank you very much to you all. If you are one of those looking at this section to see if you can find your name here, don't be disappointed, your name is in my heart.

Lastly, and most importantly, I wish to thank my parents. It must not be easy to have a son who always caused a lot of trouble and then decided to spend years getting a PhD instead of having a real job. They bore me, raised me, supported me, taught me, and loved me. To them I dedicate this thesis.

# Contents

<b>1</b>	<b>Introduction</b>	<b>17</b>
1.1	Geophysical background and applications . . . . .	19
1.2	Summary of work . . . . .	23
1.3	Summary of original contributions . . . . .	24
<b>2</b>	<b>Microscale Synthetic Schlieren</b>	<b>27</b>
2.1	Experimental set-up . . . . .	27
2.2	Data Analysis and Processing . . . . .	29
2.2.1	Mathematical derivation . . . . .	29
2.2.2	Axisymmetric inverse tomography . . . . .	34
2.3	Applications . . . . .	36
2.4	Conclusion . . . . .	43
<b>3</b>	<b>Methods of Investigation</b>	<b>45</b>
3.1	Formulation of Stratified Drag Coefficient . . . . .	45
3.2	Methods . . . . .	48
3.2.1	Drag Measurement by Time-Lapse Photography . . . . .	48
3.2.2	Wake Visualization by Microscale Synthetic Schlieren . . . . .	50
3.2.3	Numerical Model . . . . .	52
<b>4</b>	<b>Results and Discussion</b>	<b>55</b>
4.1	The drag due to stratification . . . . .	55
4.2	The wake . . . . .	63

4.3	Discussion . . . . .	64
4.3.1	Physical Mechanism for Added Drag . . . . .	70
<b>5</b>	<b>Conclusion</b>	<b>79</b>
5.1	Ideas for future work . . . . .	82
<b>A</b>	<b>A mathematical justification of suppression of vertical motion in a stratified fluid</b>	<b>83</b>

# List of Figures

2-1	A 20 mm-square mask consisting of a random pattern of 35 $\mu\text{m}$ dots.	29
2-2	Schematic of the experimental setup. . . . .	30
2-3	Discretization of the horizontal plane in the wake above a settling sphere used for tomographic inversion. The sphere is at the center. The radial density gradient perturbation is constant within each ring and zero in the outer shaded region. . . . .	36
2-4	Qualitative Synthetic Schlieren visualization of the wake of an $a = 390 \mu\text{m}$ sphere for $N = 1.31 \text{ s}^{-1}$ . The intensity is correlated with the magnitude of the density perturbation gradient. The figure is a composite of two frames (top and bottom) and the position of the sphere, added in postprocessing, is accurate to within one sphere radius.	37
2-5	Contours of the apparent horizontal pixel displacements $\Delta x$ in the wake of a 780 $\mu\text{m}$ sphere. The particle Reynolds number is $Re = 4.1$ . The portion of the sphere in the field of view has been superimposed. Data along the three horizontal transects A, B, and C are presented in Figs. 5 and 6. . . . .	38
2-6	Apparent horizontal displacements of the mask (thin line) and radial density gradient perturbation (thick line) for a 780 $\mu\text{m}$ sphere measured along transect A in Fig. 2-5. . . . .	40
2-7	Density perturbations in the wake of a 780 $\mu\text{m}$ sphere, for transects A, B, and C in Fig. 2-5. . . . .	41
2-8	Apparent horizontal displacements of the mask (thin line) and radial density gradient perturbation (thick line) for a 383 $\mu\text{m}$ sphere. . . . .	41

2-9	Apparent horizontal displacements of the mask for a $157 \mu\text{m}$ sphere. . . . .	42
3-1	(a) Schematic of a sphere settling in a linearly stratified fluid. (b) The numerical grid in the region close to the sphere. . . . .	47
3-2	(a) The settling velocity $U$ versus depth $z$ for ten replicate experiments (faint lines), along with the mean (bold line), for $a = 390 \mu\text{m}$ and $N = 2.92 \text{ s}^{-1}$ . (b) The parameter regime explored experimentally, shown in terms of $Re$ and $Fr^{-1}$ . Each experiment is represented by a continuous curve, because a particle samples decreasing $Re$ and $Fr$ as it settles into progressively denser fluid. Curves at larger $Fr$ are shorter because in a weaker stratification $U$ (and thus $Re$ and $Fr$ ) varies less over a given vertical window. All experiments were conducted at $Pr = 700$ (salt stratification). Two sphere sizes were used: $a = 196 \mu\text{m}$ (experiments 1,2,3,5,6,9,10) and $a = 390 \mu\text{m}$ (experiments 4,7,8,11). . . . .	51
4-1	The homogeneous drag coefficient $C_D^H$ measured experimentally (circles) and computed numerically (triangles), compared with the prediction from equation (3.2) (continuous line), as a function of $Re$ . . . . .	56
4-2	The normalized drag coefficient $C_D^N$ as a function of $Fr^{-1}$ for experiments (solid blue lines) and numerical simulations (symbols). The bars represent upper and lower bounds of experimental values. (b) $C_D^N$ as a function of $Ri$ for experiments (solid blue lines) and simulations (symbols). Dashed lines represent power law fits, performed separately for the experiments and each set of simulations, and color-coded accordingly. Inset: detail of $C_D^N - 1$ vs. $Ri$ in log-log scale. . . . .	58
4-3	(a, b) The numerical pressure drag coefficient $C_P^N$ and viscous drag coefficient $C_V^N$ vs. $Ri$ , along with best fit power laws (dashed lines). In all panels, dotted lines represent the theoretical prediction for homogeneous Stokes flow ( $Ri = 0$ ): $C_D^N = 1$ , $C_P^N = 1/3$ and $C_V^N = 2/3$ . . . . .	59

4-4	(a) Pressure and (b) vertical component of the tangential shear stress, along the surface of a settling sphere for $Re = 0.05$ and different $Ri$ . $Ri = 0.29, 0.43, 0.61, 0.84, 1.12, 1.45$ from top to bottom in panel (a), and from bottom to top in panel (b). $\theta = -\pi/2$ is the front of the sphere (figure 3-1). . . . .	60
4-5	(a, b) $(\nabla \wedge \omega) \cdot \mathbf{j}$ for (b) $Ri = 0.29$ ( $Re = 0.05, Fr = 0.42$ ) and (c) $Ri = 1.45$ ( $Re = 0.05, Fr = 0.19$ ). A stronger stratification results in a larger downward component of $\nabla \wedge \omega$ , hence a large viscous drag. .	61
4-6	(a, b) Vorticity field $\omega$ around the sphere for (a) $Ri = 1.25 \times 10^{-6}$ ( $Re = 0.05, Fr = 200$ ) and (b) $Ri = 1.45$ ( $Re = 0.05, Fr = 0.19$ ). (c) Radial distribution of vorticity at the equator of the sphere ( $\theta = 0$ ) for the same values of $Ri$ . Vorticity is compressed towards the sphere and enhanced at higher $Ri$ . (d) Streamlines around the sphere for $Ri = 1.25 \times 10^{-6}$ (thin lines) and $Ri = 1.45$ (thick lines) . . . . .	62
4-7	Dimensionless density field $\rho - \rho(0)$ in the wake of a settling sphere for $Ri = 0.02$ ( $Re = 2.1, Fr = 10.2$ ) obtained from (a) Microscale Synthetic Schlieren and (b) numerical simulation. . . . .	65
4-8	(a, b) Numerical isopycnal distortion at two locations around the sphere. Colorbars show $\rho - \rho(0)$ . (c) Numerical velocity field behind the sphere. For all cases, $Ri = 0.29$ ( $Re = 0.05, Fr = 0.42$ ). . . . .	66
4-9	Numerical density field $\rho - \rho(0)$ in the wake of a settling sphere for (a) $Ri = 0.29$ ( $Re = 0.05, Fr = 0.42$ ) and (b) $Ri = 1.45$ ( $Re = 0.05, Fr = 0.19$ ). Higher $Ri$ corresponds to a shorter wake and smaller isopycnal deflections. . . . .	67

4-10 (a) Horizontal and (b,c) vertical pattern displacements generated by an $a = 390 \mu\text{m}$ settling sphere, detected using Microscale Synthetic Schlieren. Colorbar units are in pixels. (a,b) $N = 1.31 \text{ s}^{-1}$ ( $Ri = 0.02, Re = 2.1, Fr = 10.2$ ); (c) $N = 2.50 \text{ s}^{-1}$ ( $Ri = 0.89, Re = 0.15, Fr = 0.4$ ). The position of the sphere, added in postprocessing, is accurate to within one sphere radius. Note the different colorbar scale in (b) and (c). . . . .	68
4-11 Numerical density field $\rho - \rho(0)$ in the wake of a settling sphere for $Ri = 0.43$ obtained from (a) $Re = 0.05, Fr = 0.34$ and (b) $Re = 0.5, Fr = 1.08$ . Note the strong difference in the wake structure, except in the region closest to the sphere. . . . .	72
4-12 (a) Density contrast $\Delta\rho$ and (b) vertical fluid velocity $w$ in the wake of a settling sphere for $Ri = 0.29$ ( $Re = 0.05, Fr = 0.42$ ). The long wake (panel a) comprises two distinct regions (panel b): the lower one travels at a speed comparable to that of the sphere ( $w \sim -1$ ). . . . .	73
4-13 The width of the wake $W$ as a function of $Ri^{-1/3}$ . . . . .	74
4-14 The length scale $\delta$ of the fluid region responsible for the added drag, as a function of $(Fr/Re)^{1/2}$ . . . . .	74
4-15 The maximum isopycnal deflection $H$ as a function of $Fr^{1/2}$ . $W$ , $\delta$ and $H$ were computed from numerical simulations as described in the text and nondimensionalized by $a$ . . . . .	75
4-16 (a) The normalized drag coefficient $C_D^N$ as a function of $Ri$ for numerical simulations at high $Re$ . (b) The normalized drag coefficient $C_D^N$ as a function of $1/Fr$ for numerical simulations at high $Re$ . Data were obtained by examining the published data in Torres <i>et al.</i> [43] visually. . . . .	76
4-17 Numerical density field $\rho - \rho(0)$ for (a) $Pr = 7$ , (b) $Pr = 100$ , (c) $Pr = 700$ . In all panels, $Ri = 1.25$ ( $Re = 0.05, Fr = 0.2$ ). . . . .	77



5-1 (a) Trajectory of an  $a = 196 \mu\text{m}$  sphere settling in stratified fluid with  $N = 1.69 \text{ s}^{-1}$ , determined experimentally (solid line) and predicted using the stratified drag coefficient from equation (4.4) (dashed line). Also shown is the trajectory of the same particle assuming a locally homogeneous drag formulation, equation (3.2) (dotted line). (b) The ratio of travel times computed using a stratified drag coefficient versus a locally homogeneous one, as a function of particle size  $a$ , density contrast  $\Delta\rho$  and stratification  $N$ . . . . . 81



# List of Tables



# Chapter 1

## Introduction

The interaction between a solid body and a fluid is one of the oldest and most fundamental problems of fluid dynamics and one that occurs in a wide range of applications, from the design of airfoils and ships to sports balls. A basic physical quantity associated with the solid-fluid interaction is the drag  $D$ , which is the resisting force the body experiences when moving relative to the fluid. It is conventional to describe the resistance to motion by a drag law via a drag coefficient  $C_D$ , which is defined as

$$C_D = \frac{D}{\frac{1}{2}\rho U^2 S}, \quad (1.1)$$

where  $\rho$  is the density of the fluid,  $U$  the velocity of the body, and  $S$  is the cross-sectional area of the body.  $S = \pi a^2$  in the case of a sphere where  $a$  is the sphere radius. From dimensional analysis of a sphere moving in a homogeneous fluid, where the fluid density is everywhere the same, one finds that  $C_D$  is a function of Reynolds number, which represents the ratio of inertial to viscous forces in the fluid, and is defined as

$$Re = \frac{Ua}{\nu}, \quad (1.2)$$

where  $\nu$  is the kinematic viscosity of the fluid. The governing equations of the fluid flow are the Navier-Stokes equations, along with appropriate boundary conditions on the solid surface. An analytical solution for a sphere traveling in a homogeneous fluid can be obtained when the transient and nonlinear terms in the Navier-Stokes

equations are negligible, corresponding to the case of inertial forces being dominated by viscous forces ( $Re \ll 1$ ). This is called Stokes flow. In this regime,  $C_D \sim 1/Re$ . A large body of experimental, theoretical, and numerical studies have contributed to determining the dependence of  $C_D$  on  $Re$  over a wide range of  $Re$  [50]. In a homogeneous fluid, the drag coefficient is directionally symmetric, i.e. the drag experienced by the sphere does not vary with the direction of motion of the sphere (e.g. horizontal vs. vertical). While the drag law is well established for a sphere moving in an homogeneous fluid, no analogous law exists for a particle settling in a stratified fluid and we lack even a basic understanding of the fluid mechanics of this scenario.

In this thesis we study the fluid dynamics of a sphere settling in a stratified fluid with a density increasing linearly with depth. The presence of stratification significantly alters the problem of particle motion in a fluid. For a given stratification agent (e.g. salt or temperature), stratification introduces an additional dimensionless parameter in the problem, the Froude number  $Fr = U/Na$ , where  $N = [(g/\rho_0)d\rho/dz]^{1/2}$  is the buoyancy frequency,  $\rho$  the fluid density,  $g$  the acceleration of gravity,  $\rho_0$  a reference fluid density, and  $d\rho/dz$  the background fluid density gradient. For a stratification without shear, the dynamics then depend on both  $Re$  and  $Fr$ . Furthermore, there is a distinct asymmetry between motion parallel and perpendicular to isopycnals (i.e. surfaces of constant density); since fluids are often vertically stratified, this corresponds to horizontal and vertical motion, respectively. The contributions of this thesis are threefold: first, we discover that drag increases due to stratification, even at low  $Re$ ; second, we formulate a drag coefficient law for a sphere settling in a linearly stratified fluid; and third, we develop a microscale Synthetic Schlieren technique, which is broadly applicable to problems in fluid mechanics and was used here to visualize the flow induced by small particles settling in stratified ambients.

## 1.1 Geophysical background and applications

The process of an object settling in a stratified fluid occurs ubiquitously in nature, yet has received little attention and remains poorly understood. While conceptually simple, the problem is somewhat paradoxical, hence intriguing: while stratification tends to suppress vertical fluid motion [52], the settling process demands it. One of the most important applications of settling in stratified ambients are environmental, chiefly the settling of marine snow aggregates through thermoclines and haloclines in oceans and lakes [26]. Marine snow particles are responsible for a net export of limiting elements from the upper ocean to greater depths and ultimately the ocean floor. Their settling time is an important parameter in models of biogeochemical fluxes. These particles can further accumulate and form thin layers of enhanced particle concentration in correspondence to strong density gradients. These layers can form their own ecosystems, triggering accumulation of organisms, and affect propagation of optical and acoustic signals. Any changes in the particle settling speed due to stratification could influence retention time of particles in the layers and hence layer formation and intensity. Marine snow and other particles of biological origin in the ocean are typically small ( $\sim 10 \mu m - 10 mm$ ) and have a small density contrast with the ambient fluid, hence settle slowly: most have a Reynolds number  $< O(1)$  [22]. Other examples include particles in the atmosphere [20], crystals settling in stratified magma chambers [32] and settling of particulate matter after nuclear explosions, hypothesized to potentially lead to nuclear winter [45]. Furthermore, there is indication that settling aggregates are themselves of major importance in channeling dissolved organic matter to the microbial loop via bacterial uptake, ultimately affecting the global carbon cycle [2].

The problem of particles moving in a viscous fluid at low Reynolds number is one of the oldest problems in fluid mechanics, reviewed by Leal [24], who includes effects of weak inertia, non-Newtonian behavior and particle deformation. The review by Davis and Acrivos [12] focuses on suspensions of particles sedimenting under the

action of gravity, where the primary question resides in the determination of the average settling speed. In this context, Blanchette and Bush [4] found that stratification reduces settling speed, locally increasing the particle concentration and thus enhancing the effects of hindered settling. Bush *et al.* [6] further explored the dynamics of a particle cloud in a stratified fluid, observing and rationalizing different modes of particle deposition.

Individual particles in a stratified fluid have been studied extensively in the case of motion parallel to isopycnals, such as particles moving horizontally through a vertical stratification, motivated by the design and operation of underwater vehicles and atmospheric flow past topography [36, 37, 17, 47]. The tendency of stratification to suppress vertical motion [52] drives flow primarily around, rather than over, a horizontally-moving three-dimensional body, while a two-dimensional body blocks a horizontal layer of fluid, the length of which scales linearly with the Richardson number  $Ri = Re/Fr^2$  [44]. To avoid confusion, we note that another dimensionless quantity in oceanography,  $Ri = (N/(dU/dz))^2$ , is also referred to as the Richardson number. While both definitions ultimately refer to the relative importance of buoyancy and shear forces, hence justifying the common name "Richardson number", the physical configuration is quite different in the two cases, as  $Ri = (N/(dU/dz))^2$  refers to a stratified water column subject to large-scale vertical shear  $dU/dz$  and is used to predict the stability of this scenario. Here, instead, the shear forces entering the definition of  $Ri = a^3 N^2 / (\nu U)$  arise from viscous shear generated by the sphere-induced flow. At moderate to high  $Re$ , a body moving in a stratified fluid generates internal waves, which contribute to enhance the drag on the body. Scase and Dalziel [35] used asymptotic approximations to calculate the drag on a sphere being towed through a uniformly stratified fluid, and found the internal wave drag to be significant relative to viscous drag for  $Re \geq O(10^3)$  and  $1 \leq Fr \leq 3$ . Lofquist and Purtell [25] also measured an internal-wave induced increase in drag for  $150 \leq Re \leq 5000$ , but further observed a decrease in drag due to suppression of turbulence in the wake. Greenslade [18] derived a drag law ( $C_D$  as a function of  $Fr$ ) for a horizontally moving sphere,



which says that at small  $Fr$  the added drag increases with increasing  $Fr$ , and attains a maximum at a value of  $Fr$  in the approximate range of (0.2, 0.5), then decreases with increasing  $Fr$ , at least up to  $Fr \approx 3$ , and remains approximately constant for larger  $Fr$ . The theory agrees reasonably well with experimental data [25] except for  $Fr \approx 1$ .

Considerably less work exists vertically-moving bodies in stratified fluids. The simplest configuration, a two-layer fluid, was first investigated by Srđić-Mitrović *et al.* [38], who measured the drag on a sphere settling through a thin density interface for  $1.5 < Re < 15$ . Their study revealed up to an order of magnitude increase in drag over the homogeneous case for  $3 < Fr < 10$ . The added drag resulted from the buoyancy of a tail of light fluid dragged down by the sphere. For the same configuration, Abaid *et al.* [1] found a regime in which the sphere ‘levitates’, briefly reversing direction after crossing the interface. For a body smaller than the vertical extent of the stratification, consideration of a continuous stratification is more appropriate than a sharp interface; the simplest case being a linear stratification. Torres *et al.* [43] numerically investigated the case of a sphere in the parameter regime  $25 \leq Re \leq 100$  and  $0.2 \leq Fr \leq 200$ , finding  $C_D$  to strongly increase with  $Fr^{-1}$  for  $Fr < 20$ . The added drag was due to a rear buoyant jet, predicted by Eames *et al.* [13] for an inviscid and non-diffusive fluid, associated with the return of isopycnals to their neutral density position. The existence of this jet, and the associated suppression of rear vortices, was supported by shadowgraph experiments at  $Re \sim 800$  [28]. An increase of  $C_D$  with  $Fr^{-1}$  was also observed by Higginson *et al.* [19] for the related problem of a freely-rising horizontal grid of bars at  $1000 \leq Re \leq 3000$  and  $0.03 \leq Fr \leq 0.22$ , and rationalized in terms of the buoyancy of displaced fluid in the wake of the grid. Although internal waves can exist for moderate to high  $Re$  [48], in the aforementioned studies they were found not to contribute to drag. While a theoretical analysis Zvirin and Chadwick [53] suggests that stratification enhances drag even at  $Re \ll 1$ , predicting a dependence of  $C_D$  on  $Ri^{1/3}$ , there is a dearth of quantitative experimental data at small Reynolds numbers. Thus it still remains unclear whether settling particles experience added drag at  $Re = O(1)$  and, if so, how

this drag scales with stratification.

A full understanding of these processes requires the ability to visualize and understand the fluid mechanics of a stratified system at these small scales. Optical techniques based on the relation that typically exists between density and refractive index have long been used to visualize perturbations in a stratified fluid. Examples include the classic Schlieren [42] and Moiré fringe techniques [7]. Synthetic-Schlieren is a digital implementation of this idea that was recently developed for quantitative investigations of two-dimensional, linear internal-wave fields [10, 40], and qualitative visualization of nonlinear internal waves [32]. A similar digital technique, Background Oriented Schlieren, as reviewed by Venkatakrishnan and Meier [46], has been applied to study the dynamics of compressible vortices [34]. Most recently an axisymmetric formulation of Synthetic Schlieren has been developed [29] and used to study internal waves excited by a vertically oscillating sphere [15]. This approach exploits radial symmetry and inverse tomographic techniques to study axisymmetric perturbations in a stratified fluid.

To date, investigations using Synthetic Schlieren have been concerned with phenomena occurring on lengthscales in the range of 10 mm to 1 m. However, many processes in stratified fluids occur at scales of microns to millimeters, in particular ecologically and environmentally relevant phenomena in the ocean, such as marine snow. To study microscale particles settling in a homogenous fluid, it is convenient to scale up the size of an experiment, using a more viscous fluid to maintain dynamic similarity. This is not feasible in the presence of stratification, however, because one cannot appropriately scale diffusion of the stratifying agent. Therefore, the settling of microscale particles in a stratified ambient must indeed be studied on the microscale, demanding challenging experiments, of which there are few. One example is the study of Srdić-Mitrović *et al.* [38] who tracked submillimeter spheres traversing sharp density interfaces.

To address our limited knowledge of processes involving small-scale disturbances in stratified fluids, we herein extend Synthetic Schlieren to submillimeter scales. In so doing, we operate on a scale two orders of magnitude smaller than any prior studies using this method. This presents practical challenges: smaller size particles require increasing magnification and generate ever weaker signals, which are eventually overwhelmed by noise. We used our experimental arrangement to study the flow structure in the wake of settling spheres, down to a diameter of  $157\ \mu\text{m}$ . Furthermore, for this process we found that perturbations of the horizontal density gradient far exceed those of the vertical gradient, requiring modification of the axisymmetric method.

## 1.2 Summary of work

In this thesis we present a combined experimental, numerical and theoretical analysis of the drag experienced by a sphere settling in a linearly stratified fluid at low  $Re$ . This work complements previous experimental and numerical work at higher  $Re$  [19, 43], and step-like stratification [38, 1]. For the experimental component of the study, we developed a new flow visualization technique called microscale Synthetic Schlieren, which allowed us to visualize the density field around a microscale sphere settling in a stratified fluid. We further employed time-lapse photography to measure the settling speed of a sphere and hence compute its drag. Finally, conclusions were supported by numerical simulations. The main finding of this work is that stratification increases the hydrodynamic drag, even at low Reynolds numbers. We found that, while the problem in general depends on both Reynolds number  $Re$  and Froude number  $Fr$ , the increase in drag scales with a unique combination of  $Re$  and  $Fr$  through the Richardson number  $Ri = Re/Fr^2$ . From the analysis of isopycnal (surfaces of constant density) deformation around the sphere, we elucidated the physical mechanism responsible for the drag increase, and found it to be drastically different from previously proposed mechanisms in different flow regimes. Based on the experimental and numerical results, we derived a scaling argument to rationalize the drag

coefficient law.

This thesis is structured as follows. In Chapter 2 we provide the formulation of microscale Synthetic Schlieren, and investigate the applicability and limitations of the method. The materials in this chapter were published in *Experiments in Fluids* in 2006 [51]. In Chapter 3 we provide an outline of all the methods of investigation, including time-lapse photography and numerical simulations. In Chapter 4 we present the results and discussion, while Chapter 5 contains conclusions and suggestions for future work. The materials in Chapter 3, 4, and 5 are presented in a paper titled *Enhanced Drag of a Sphere Settling in a Stratified Fluid at Small Reynolds number*, which has been submitted to the *Journal of Fluid Mechanics*.

### 1.3 Summary of original contributions

The key original contributions of this thesis, representing work that was performed by myself and that goes beyond existing literature, are as follows:

- Developed microscale Synthetic Schlieren technique. Demonstrated that Synthetic Schlieren could be extended to microscale fluid mechanics problems ( $\sim 100 \mu m$ ). Developed a novel formulation to analyze radial density perturbations and corrected mistakes in the mathematical formulations of previous studies.

- Visualized the wake structure behind a settling sphere by microscale Synthetic Schlieren.

- Performed the first experimental study to quantify the drag coefficient for a sphere settling in a stratified fluid at low Reynolds numbers, and established the dependence of the drag coefficient  $C_D$  on Richardson number  $Ri$ . Elucidated the manner in which stratification enhances drag, hence reduces settling speed, at low

Reynolds numbers.

- Proposed an empirical law for the drag coefficient in a stratified fluid.
- Proposed a novel physical mechanism responsible for the observed added drag and corroborated it with a scaling argument.



# Chapter 2

## Microscale Synthetic Schlieren

In this chapter, we will first introduce the experimental set-up used for microscale Synthetic Schlieren, then we present the data analysis and processing routines, and lastly we discuss some results of microscale Synthetic Schlieren, along with its applicability and limitations. The materials in this chapter were previously published in a paper in *Experiments in Fluids* [51].

### 2.1 Experimental set-up

The experiments were performed in a 0.48 m high, 63 mm long and 25 mm wide perspex tank, with 5.4 mm thick walls, standing on a vibration-damped table, as shown in Figure 2-2. The tank was filled with linearly stratified salt water using a double-bucket system [30], and left to stand for several hours to allow dissipation of any residual flows. Several spherical density floats (American Density Floats) with densities covering the range 1010.0 to 1060.0 kg m<sup>-3</sup> in intervals of 10.0 kg m<sup>-3</sup> were then released into the tank to measure the vertical density gradient  $d\rho/dz$ . The small size of the floats (7 mm diameter) ensured that the density gradient was not distorted by their presence. Regular spacing of the vertical positions of the floats (i.e. their neutral buoyancy heights) confirmed the linearity of the density profile. The corresponding density gradient was determined from a linear fit to this data. There was

no discernible motion of the floats, demonstrating the absence of any convection in the tank that could have affected the experimental results.

Experiments were performed using polystyrene spheres of diameter 3.16 mm and 750, 383 and 157  $\mu\text{m}$ , having density  $1050 \text{ kg m}^{-3}$ . A 3-stage micro-manipulator mounted on top of the experimental tank facilitated the accurate deposition of the spheres, ensuring their release in the center of the tank and subsequent passing through the desired observation window as they settled. The micro-manipulator held a partially submerged conical injector (a 1 ml pipette) with an entrance diameter of 9.5 mm and an exit diameter of 3.3 mm, through which the spheres were released into the tank. The 3.16 mm and 750  $\mu\text{m}$  spheres were deposited into the conical injector using a pair of tweezers. This was not feasible for the 383 and 157  $\mu\text{m}$  spheres, which were instead mixed in very dilute quantities into a water sample, and then released into the conical injector using a 1 ml pipettor.

To image the wake of the settling spheres using Synthetic Schlieren, a 20 mm-square mask consisting of a random pattern of 35  $\mu\text{m}$  dots was printed on transparency film using a high-resolution image-setter (Figure 2-1). The same mask was used for all experiments. The pattern was mounted a distance  $B=83$  mm behind the back wall of the tank, and imaged at 20 frames per second using a PCO 1600 CCD camera, operating at a resolution of 800 x 600 pixels. The camera was mounted on a Nikon SMZ 1000 stereo-microscope fitted with a P-Achro 0.5X objective, positioned a distance  $L=189$  mm in front of the mask, corresponding to the maximum working distance. Magnification factors of 7.5X, 10X and 15X were used, corresponding to observation windows of 15.2 x 11.4, 11.5 x 8.6, and 7.6 x 5.7  $\text{mm}^2$ , respectively.

Images were captured using IPLab (Scanalytics) and the apparent displacements of the mask, caused by perturbations of the density stratification, were determined using DigiFlow [11]. To minimize the effect of thermal fluctuations, a thermal isolation tunnel was placed between the microscope and the tank, and the reference image



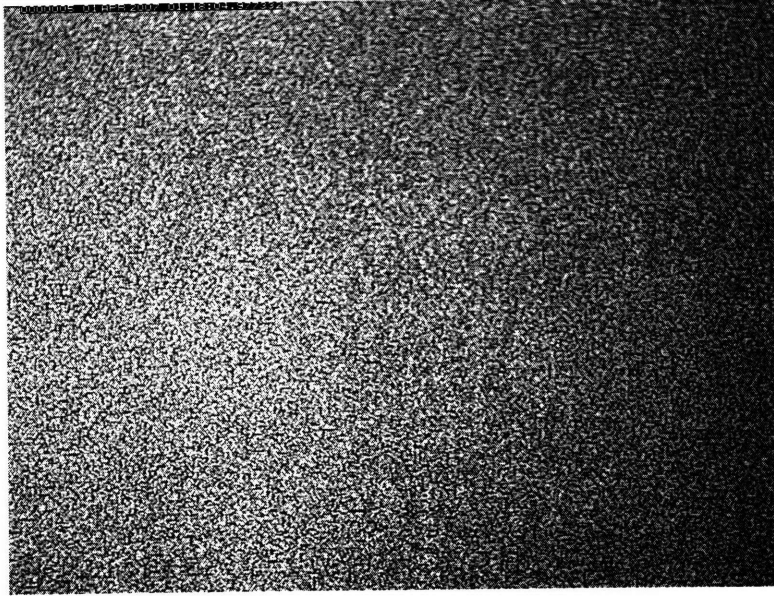


Figure 2-1: A 20 mm-square mask consisting of a random pattern of  $35 \mu\text{m}$  dots.

required by Synthetic Schlieren was an average of the first ten frames captured prior to the settling sphere entering the observation window.

## 2.2 Data Analysis and Processing

We begin by reviewing the axisymmetric Synthetic Schlieren technique detailed in Onu et al. [29], before presenting the inverse tomographic method, with modifications relevant to studying the wake of a settling sphere.

### 2.2.1 Mathematical derivation

The path followed by a light ray in a stratified fluid satisfies Fermat's variational principle

$$\delta \int n(x, y, z) ds = 0. \quad (2.1)$$

Here  $s$  is the along-the-light-ray coordinate and  $n(x, y, z)$  is the refractive index field that is a function of across-tank ( $x$ ), along-tank ( $y$ ) and vertical coordinates ( $z$ ) (see

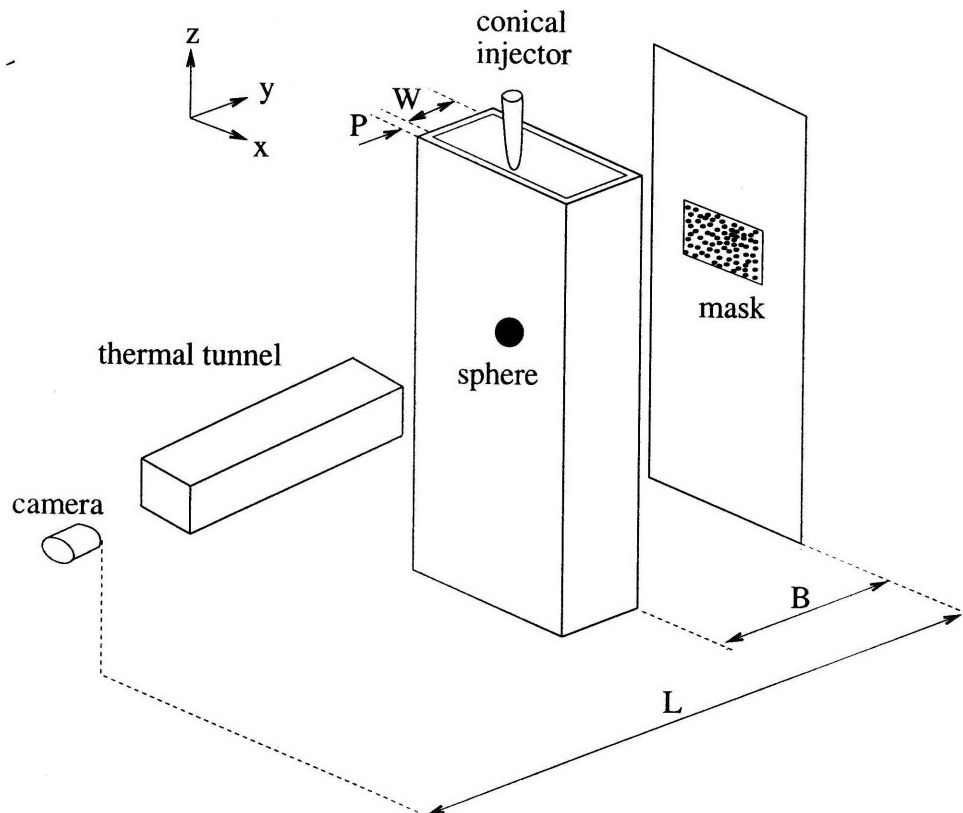


Figure 2-2: Schematic of the experimental setup.

Figure 2-2). Assuming the tangent to the light ray path always has a component in the  $y$  direction, the path can be described by  $x(y)$  and  $z(y)$ : the former satisfies

$$\frac{d^2x}{dy^2} = \left[ 1 + \left( \frac{dx}{dy} \right)^2 + \left( \frac{dz}{dy} \right)^2 \right] \frac{1}{n} \frac{\partial n}{\partial x}, \quad (2.2)$$

[49], and the latter the same equation with  $x$  and  $z$  interchanged. Provided that a light ray remains sufficiently parallel to the  $y$  direction, the nonlinear terms in (2.2) become negligible (for our set-up these are  $O(10^{-2})$  or less), and the equations for  $x(y)$  and  $z(y)$  decouple. Since we anticipate horizontal density gradient perturbations, and thus horizontal refractive index gradient perturbations, to greatly exceed vertical ones (except perhaps in a small region in front of the sphere where isopycnals are compressed), our focus will be on the horizontal deflection of a light ray. By direct integration the  $x$ -component of a light-ray path is then

$$x(y) = x_i + y \cot \phi_i + \frac{1}{n_0} \int_0^y \int_0^{\hat{y}} \frac{\partial n}{\partial x} d\hat{y} d\hat{y}, \quad (2.3)$$

where  $x_i$  and  $\phi_i$  are the location and angle of incidence in the horizontal plane at the point a light ray enters the tank, respectively.

Consider the path followed by a light ray from the camera to the tank, which then arcs through the stratified fluid and eventually incidents on the random pattern of dots. Note that the light ray itself travels from the random pattern of dots to the camera, but back-tracking the light ray path is geometrically more convenient. We decompose the quiescent refractive index field  $n$  into  $n = n_o + n_b$ , where  $n_o$  is the reference index of the medium,  $n_b$  is the background index gradient associated with the background density gradient. With the settling of a sphere, the disturbed refractive index field  $n_d$  becomes  $n = n_o + n_b + n'$ , where  $n'$  is the index field perturbations caused by the settling of the sphere. We assume that  $n_b$  and  $n'$  are small compared with  $n_o$ .

Without the settling sphere, the light ray path is given by equation (2.3) for  $0 \leq y \leq$

$W$  and given by equation (2.4) for  $W < y$ .

$$x(y) = x_i + W \tan \phi_i + \int_0^W \int_0^{\hat{y}} \frac{1}{n} \frac{\partial n}{\partial x} d\hat{y} d\hat{y} + P \tan \phi_P + B \tan \phi_B, \quad (2.4)$$

Here  $x_i$  and  $x_B$  are the horizontal positions of the light ray as it enters the interior of the tank and that of the light ray leaving the tank respectively.  $\phi_i$ ,  $\phi_W$ ,  $\phi_P$ , and  $\phi_B$  are the angles made between the light ray and the horizontal when the light ray enters the interior of the tank, incidents on the tank wall as it leaves the interior of the tank, travels inside the tank wall, and after it leaves the tank respectively.  $\tan \phi_W$  can be obtained by differentiating equation (2.3) with respect to  $y$  and evaluate at  $y = W$ .

$$\tan \phi_W = \left. \frac{dx}{dy} \right|_{y=W} = \tan \phi_i + \int_0^W \frac{1}{n} \frac{\partial n}{\partial x} d\hat{y}, \quad (2.5)$$

By assuming that the light ray remains approximately parallel to the horizontal,  $\tan \phi \approx \phi$  and  $\sin \phi \approx \phi$ , where  $\phi$  is the angle between the light ray and horizontal. By applying the Snell's law as the light ray leaves the interior of the tank and entering the tank wall, and as the light ray leaves the tank wall respectively:

$$\phi_P = \phi_W \frac{n_o}{n_p} \quad (2.6)$$

$$\phi_B = \phi_P \frac{n_p}{n_a} = \phi_W \frac{n_o}{n_a} \quad (2.7)$$

Since  $\tan \phi_P \approx \phi_P$  and  $\tan \phi_B \approx \phi_B$ , equation (2.4) can be written as

$$x(y) = x_i + W \tan \phi_i + \int_0^W \int_0^{\hat{y}} \frac{1}{n} \frac{\partial n}{\partial x} d\hat{y} d\hat{y} + \left( P \frac{n_o}{n_p} + B \frac{n_o}{n_a} \right) \phi_W, \quad (2.8)$$

by using equation (2.5) and that  $\tan \phi_W \approx \phi_W$

$$\begin{aligned} x(y) = & x_i + W \tan \phi_i + \int_0^W \int_0^{\hat{y}} \frac{1}{n} \frac{\partial n}{\partial x} d\hat{y} d\hat{y} \\ & + \left( P \frac{n_o}{n_p} + B \frac{n_o}{n_a} \right) \left( \tan \phi_i + \int_0^W \frac{1}{n} \frac{\partial n}{\partial x} d\hat{y} \right) \end{aligned} \quad (2.9)$$

Similarly, the light ray path  $x_d(y)$  under the disturbance of a settling sphere is given

by

$$\begin{aligned}
x_d(y) &= x_i + W \tan \phi_i + \int_0^W \int_0^{\hat{y}} \frac{1}{n_d} \frac{\partial n_d}{\partial x} d\hat{y} d\hat{y} \\
&\quad + \left( P \frac{n_o}{n_p} + B \frac{n_o}{n_a} \right) \left( \tan \phi_i + \int_0^W \frac{1}{n_d} \frac{\partial n_d}{\partial x} d\hat{y} \right), \tag{2.10}
\end{aligned}$$

The apparent horizontal displacement  $\Delta x$  is given by

$$\begin{aligned}
\Delta x &= -(x_d - x) \\
&= \int_0^W \int_0^{\hat{y}} \frac{1}{n} \frac{\partial n}{\partial x} - \frac{1}{n_d} \frac{\partial n_d}{\partial x} d\hat{y} d\hat{y} \\
&\quad + \left( P \frac{n_o}{n_p} + B \frac{n_o}{n_a} \right) \int_0^W \frac{1}{n} \frac{\partial n}{\partial x} - \frac{1}{n_d} \frac{\partial n_d}{\partial x} d\hat{y} \tag{2.11}
\end{aligned}$$

Since

$$\frac{1}{n} \frac{\partial n}{\partial x} - \frac{1}{n_d} \frac{\partial n_d}{\partial x} \approx -\frac{1}{n_o} \frac{\partial n'}{\partial x} \tag{2.12}$$

hence

$$\Delta x = - \int_0^W \int_0^{\hat{y}} \frac{1}{n_o} \frac{\partial n'}{\partial x} d\hat{y} d\hat{y} - \left( P \frac{n_o}{n_p} + B \frac{n_o}{n_a} \right) \int_0^W \frac{1}{n_o} \frac{\partial n'}{\partial x} d\hat{y}, \tag{2.13}$$

If we assume the index perturbation  $n'$  is two dimensional,  $P = 0$  and  $n_o/n_a = 1$ , then , equation (2.13) becomes

$$\Delta x = -\frac{1}{2} W(W + 2B) \frac{1}{n_o} \frac{\partial n'}{\partial x} \tag{2.14}$$

Making use of the relation  $\frac{1}{n_o} \frac{\partial n}{\partial x} = \frac{\gamma g}{\rho_0} \frac{\partial \rho}{\partial x}$ , the apparent horizontal displacement  $\Delta x$  of a feature in the mask due to a perturbation  $\rho'(x, z)$  of the density field in a tank of width  $W$  is

$$\Delta x = -K_1 \int_0^W \frac{\partial \rho'}{\partial x} dy - K_2 \int_0^W \int_0^y \frac{\partial \rho'}{\partial x} d\hat{y} dy. \tag{2.15}$$

Here  $K_1 = \frac{\gamma g n_o}{\rho_0} \left( \frac{B}{n_a} + \frac{P}{n_p} \right)$ ,  $K_2 = \frac{\gamma g}{\rho_0}$ ,  $P$  is the thickness of the container walls,  $n_a$  and  $n_p$  are the refractive indices of air and the tank walls, respectively,  $\rho_0$  and  $n_o$  are the

characteristic density and refractive index of salt-water,  $g$  is the acceleration of gravity, and  $\gamma=1.878 \text{ m}^{-1}\text{s}^2$  for salt-water <sup>1</sup>. For an axisymmetric disturbance extending over a characteristic length-scale  $V$ , the first term in equation (2.15) scales as  $BV$  (for  $B \gg P$ ), whereas the second term scales as  $V^2$ . For microscale applications,  $V \ll B$  and the signal is dominated by the first integral.

In general, equation (2.15) is fully three-dimensional, but in the special case of an axisymmetric disturbance it can be solved using two-dimensional techniques. This was demonstrated for the axisymmetric wavefield generated by an oscillating sphere, where  $\frac{\partial \rho'}{\partial z}$  was determined from apparent vertical displacements [29]. Here we use a modified version of the same technique to measure  $\frac{\partial \rho'}{\partial x}$ , which itself is not axisymmetric, but can be derived from the axisymmetric quantity  $\frac{\partial \rho'}{\partial r} = \frac{r}{x} \frac{\partial \rho'}{\partial x}$ . The integral equation we consider is therefore

$$\Delta x = -K_1 \int_0^W \frac{\partial \rho'}{\partial r} \frac{x}{r} dy - K_2 \int_0^W \int_0^y \frac{\partial \rho'}{\partial r} \frac{x}{r} d\hat{y} dy. \quad (2.16)$$

This provides a means for determining  $\frac{\partial \rho'}{\partial r}$  from measured apparent displacements  $\Delta x$  of a mask, as described in the following section.

## 2.2.2 Axisymmetric inverse tomography

First, we consider a  $2V \times 2V$  horizontal cross-section of the wake behind a settling sphere, centered on the line of axisymmetry, and outside of which density perturbations are negligible. This domain is discretized into a series of rings in the manner shown in Figure 2-3.

---

<sup>1</sup>In deriving (2.15) we have corrected a sign in the presentation of the formulation in [10], [15], [29], and [40]; the results in those papers remain unaffected (S. Dalziel, pers. comm, 05/06; B. Sutherland, pers. comm., 05/06). We have also included a multiplicative factor  $1/n_0$  on the right-hand side of (2.15) that is missing in [15] and [29]

Consider the  $N$ -component vector of apparent horizontal displacements

$$\mathbf{D} = [\Delta x(x_1), \Delta x(x_2), \dots, \Delta x(x_N)], \quad (2.17)$$

in which  $x_i$  are the evenly spaced horizontal locations at which apparent displacements are measured. Since the wake structure is axisymmetric,  $\frac{\partial \rho'}{\partial r}$  can be discretized as the  $N$  component vector

$$\mathbf{Q} = \left[ \frac{\partial \rho'}{\partial r}(R_0), \frac{\partial \rho'}{\partial r}(R_1), \dots, \frac{\partial \rho'}{\partial r}(R_{N-1}) \right], \quad (2.18)$$

where  $R_i$  represents the mean of the inner and outer radii of the  $i$ -th ring and we have assumed  $\frac{\partial \rho'}{\partial r} = 0$  in the outermost (shaded) region in Figure 2-3. Therefore, the two integrals in equation (2.16) can be approximated at  $x_i$  by

$$\int_{-V}^V \frac{\partial \rho'}{\partial r} \frac{x}{r} dy \simeq 2 \sum_{j=i-1}^{N-1} \frac{\partial \rho'}{\partial r}(R_j) \frac{x_i}{R_j} \Delta y_{ij} = \mathbf{G}_1 \mathbf{Q}, \quad (2.19)$$

and

$$\int_{-V}^V \int_{-V}^y \frac{\partial \rho'}{\partial r} \frac{x}{r} d\hat{y} dy \simeq \sum_{k=1}^{2N} \Delta \tilde{y}_{ik} \sum_{j=1}^k \Delta \tilde{y}_{ij} \frac{\partial \rho'}{\partial r}(\tilde{R}_j) \frac{x_i}{\tilde{R}_j} = \mathbf{G}_2 \mathbf{Q}, \quad (2.20)$$

where  $\Delta y_{ij}$  is the length of the horizontal transect in ring  $j$  (the central ring is labeled 0) corresponding to position  $x_i$ , as shown in Figure 2-3;  $\Delta \tilde{y}_{ij} = \Delta y_{i(j-N-1)}$  and  $\tilde{R}_j = R_{j-N-1}$  if  $j \geq N + i$ ,  $\Delta \tilde{y}_{ij} = \Delta y_{i(N-j)}$  and  $\tilde{R}_j = R_{N-j}$  if  $j \leq N - i + 1$ , and  $\Delta \tilde{y}_{ij} = 0$  otherwise; and  $\mathbf{G}_1$  and  $\mathbf{G}_2$  are  $N \times N$  mesh-dependent matrices.

The integral equation (2.16) is thus converted into the discrete problem

$$\mathbf{D} = -(K_1 \mathbf{G}_1 + K_2 \mathbf{G}_2) \mathbf{Q}, \quad (2.21)$$

which can readily be solved by inverting the matrix  $K_1\mathbf{G}_1 + K_2\mathbf{G}_2$ . Before analyzing the experimental data, we successfully tested the numerical implementation of this algorithm for the axisymmetric density perturbation  $\rho' = e^{-r^2}$ , for which equation (2.16) can be solved analytically.

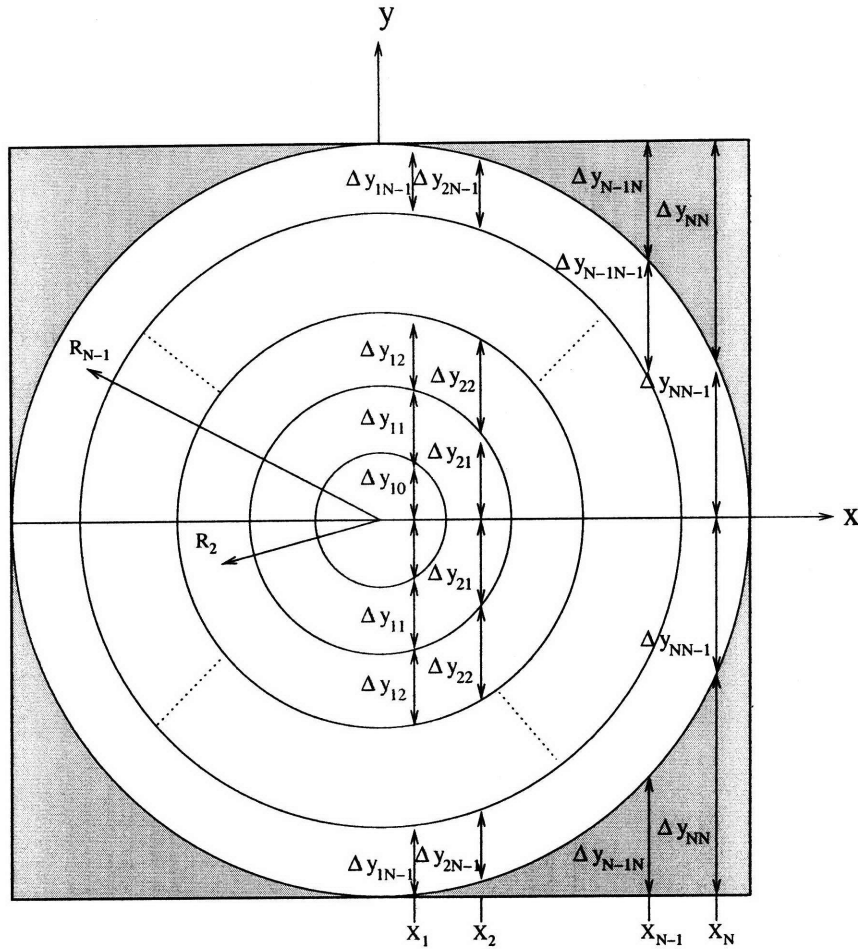


Figure 2-3: Discretization of the horizontal plane in the wake above a settling sphere used for tomographic inversion. The sphere is at the center. The radial density gradient perturbation is constant within each ring and zero in the outer shaded region.

## 2.3 Applications

Our first application of the microscale Synthetic Schlieren technique was for a 780  $\mu\text{m}$  diameter sphere settling in a stratification with  $N = 1.31 \text{ s}^{-1}$ , and  $Re = 4.1$ .



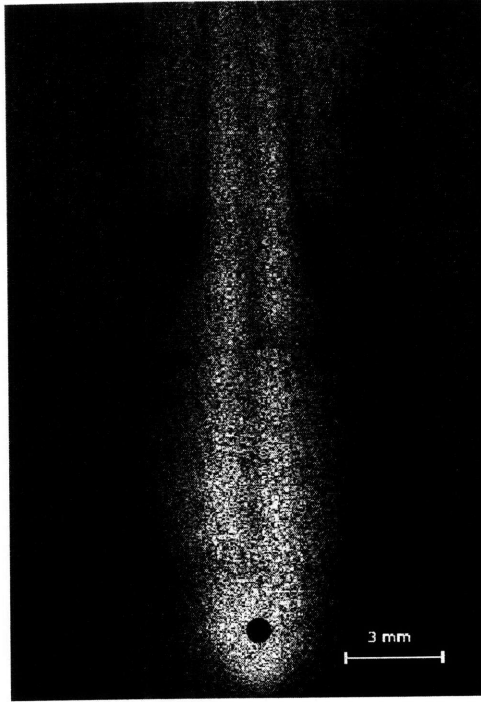


Figure 2-4: Qualitative Synthetic Schlieren visualization of the wake of an  $a = 390 \mu\text{m}$  sphere for  $N = 1.31 \text{ s}^{-1}$ . The intensity is correlated with the magnitude of the density perturbation gradient. The figure is a composite of two frames (top and bottom) and the position of the sphere, added in postprocessing, is accurate to within one sphere radius.

For these experiments we used 7.5X magnification, corresponding to a resolution of  $19 \mu\text{m}/\text{pixel}$ . Figure 2-4 shows an example of the wake behind the sphere, obtained by subtraction of the reference image. This technique is commonly referred to as qualitative Synthetic Schlieren [10], and approximates the magnitude of the density gradient perturbations. Despite this relatively crude processing, the structure of the wake is already evident. It is highly symmetric about the dark vertical centerline, where distortions of the pattern are small. Furthermore, the wake is approximately 5 mm wide and more than 22 mm long, greatly exceeding the size of the sphere.

The structure of the wake, in particular its symmetry, is even more evident in Figure 2-5, which presents a contour plot of the apparent horizontal displacements  $\Delta x$  of the mask. This data was obtained using the pattern-matching algorithms of [11], with an interrogation-window of 19 pixels and a window-spacing of 16 pixels,

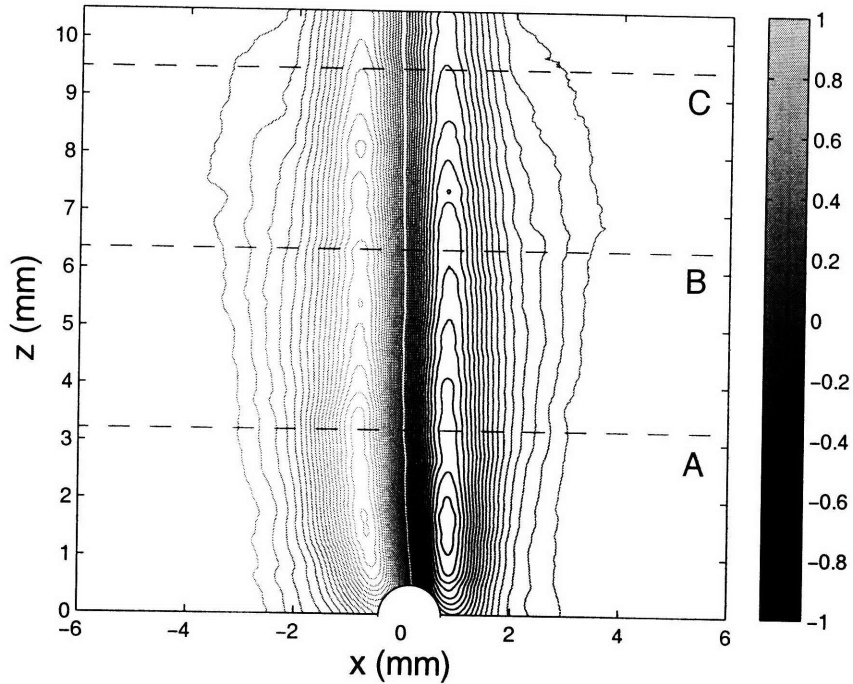


Figure 2-5: Contours of the apparent horizontal pixel displacements  $\Delta x$  in the wake of a  $780 \mu\text{m}$  sphere. The particle Reynolds number is  $Re = 4.1$ . The portion of the sphere in the field of view has been superimposed. Data along the three horizontal transects A, B, and C are presented in Figs. 5 and 6.

corresponding to approximately 20 data points across the width of the wake. A spatial zero-phase, low-pass Butterworth filter was used to remove high-frequency noise prior to axisymmetric processing. Characteristic horizontal displacements were on the order of 0.5 pixels ( $9.5 \mu\text{m}$ ), demonstrating good operating conditions for the pattern matching techniques, which are accurate to better than 0.1 pixels [10].

One practical difficulty of Synthetic Schlieren at the microscale is that the small depth of focus of the video-microscope requires the sphere to be very close to the mask (small  $B$ ) in order to have both in focus. This conflicts with the demand that the sphere be sufficiently far from the mask to generate a strong enough signal, as discussed earlier in regards to equation (2.15), effectively precluding focusing on both the mask and the sphere at the same time. Thus the sphere itself cannot be clearly resolved in the image. While one could envisage an experimental set-up that includes

a second, synchronized video-microscope focused on the sphere and capable of simultaneously tracking its location, we could visually determine the position of the sphere in each raw image to within one sphere radius. For the data in Figure 2-5, the center of the sphere was approximately  $(x,z)=(0.3,-0.1)$  mm.

The apparent horizontal displacements  $\Delta x$  measured along a cross-section of the wake approximately four diameters above the sphere, indicated by the dashed line A in Figure 2-5, are presented in Figure 2-6. The horizontal density gradient perturbation  $\frac{\partial \rho'}{\partial r}$  was then obtained from  $\Delta x$  using the axisymmetric algorithm detailed in section 3. Figure 2-6 shows that the magnitude of  $\frac{\partial \rho'}{\partial r}$  ( $\sim 220 \text{ kg m}^{-4}$ ) is greater than the background vertical stratification ( $\sim 180 \text{ kg m}^{-4}$ ), implying strong distortions of isopycnals by the settling sphere. In contrast to previous studies of internal waves, it is interesting to recognize that Synthetic Schlieren can reliably detect such dramatic nonlinear distortions of the background stratification. This is due to the region of influence of the sphere being highly localized and therefore still generating only a weak deflection of the light ray passing through the tank. In obtaining  $\frac{\partial \rho'}{\partial r}$ , we enforced  $\Delta x = 0$  at either end of the profile, smoothly tapering it off over the last 10 pixels. This was done to avoid far-field apparent displacements  $\Delta x$ , which are on the order of the background noise level (0.02 pixels), being amplified by the axisymmetric processing and deteriorating the density perturbation profile.

Integrating  $\frac{\partial \rho'}{\partial r}$  along a radial transect and adding the background stratification yields the perturbed density  $\rho$  at a given cross-section of the wake. This is illustrated in Figure 2-7 for the transects A, B, and C, indicated in Figure 2-5, which are 4, 8, and 12 diameters above the sphere, respectively. The accuracy of the method is supported by the fact that, after integration across the wake, only a minor density mismatch exists between the far field on the left and the right of the sphere ( $<0.016 \text{ kg m}^{-3}$ ). As one might expect, Figure 2-7 shows that lighter fluid is dragged downwards by the settling sphere. The fluid at the center of the wake has been dragged down a distance  $\rho' / \frac{\partial \rho}{\partial z}$ , corresponding to 1.9 mm for transect A, 1.6 mm for transect

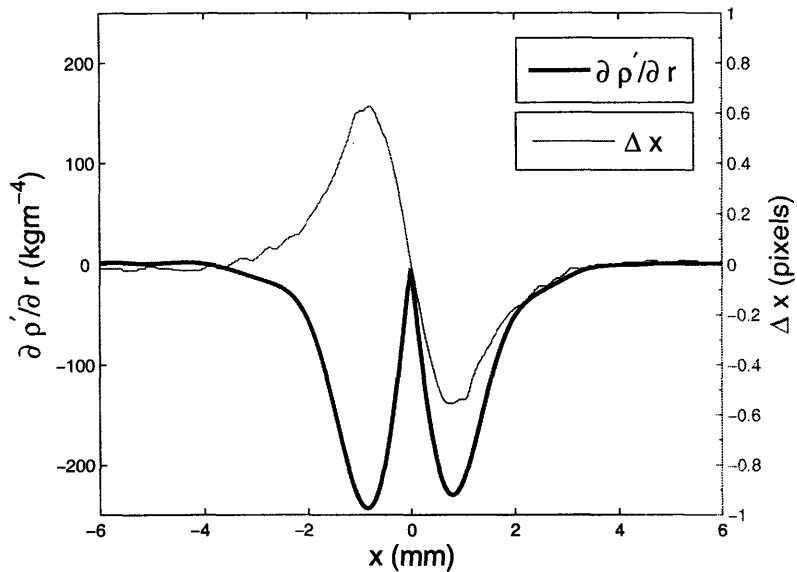


Figure 2-6: Apparent horizontal displacements of the mask (thin line) and radial density gradient perturbation (thick line) for a  $780 \mu\text{m}$  sphere measured along transect A in Fig. 2-5.

B, and 1.2 mm for transect C. We note that this corresponds to about 1 sphere diameter. The three transects show that the density perturbations diminish along the wake, although Figure 2-5 reveals that there is a 2 mm region immediately behind the sphere in which the opposite is true.

To test the operational limits of our setup, we performed additional experiments with smaller spheres, of diameter 383 and  $157 \mu\text{m}$ , using 10X and 15X magnification, respectively. The apparent horizontal displacements and the corresponding radial density gradient perturbations measured four diameters above a  $383 \mu\text{m}$  sphere settling in a stratification with  $N = 1.17 \text{ s}^{-1}$  are shown in Figure 2-8. The signature of the wake can still clearly be detected by Synthetic Schlieren, although it is noticeably weaker, with apparent displacements that are about one quarter of those for the  $780 \mu\text{m}$  sphere. After processing, the resulting radial density gradient perturbations are smaller by roughly the same ratio.

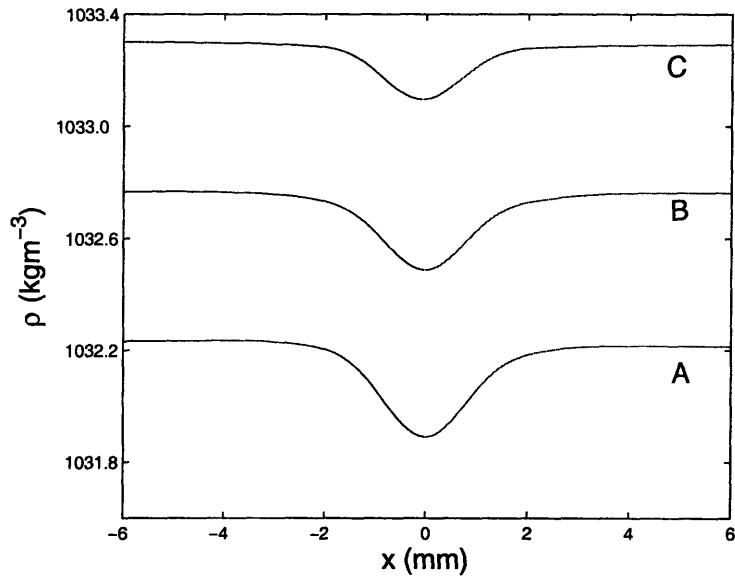


Figure 2-7: Density perturbations in the wake of a 780  $\mu\text{m}$  sphere, for transects A, B, and C in Fig. 2-5.

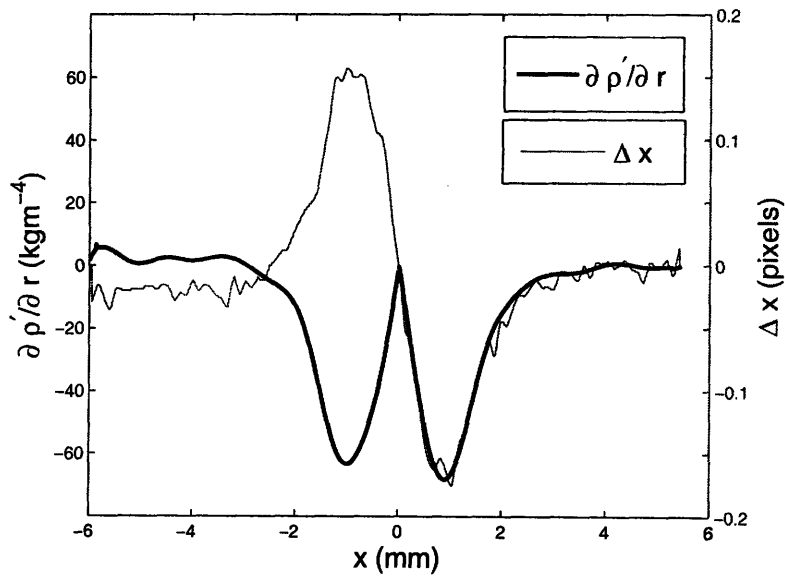


Figure 2-8: Apparent horizontal displacements of the mask (thin line) and radial density gradient perturbation (thick line) for a 383  $\mu\text{m}$  sphere.

On an even smaller scale, cross-sectional data of the maximum detected horizontal displacement anywhere along the wake of a  $157\ \mu\text{m}$  sphere is presented in Figure 2-9. While there is evidence of antisymmetric apparent displacements (highlighted by the dashed line that guides the eye) similar to those in Figures 2-6 and 2-8, the magnitude of this signal is significantly smaller than for the larger spheres. Furthermore, the signal is compromised by the experimental noise, indicating that a  $157\ \mu\text{m}$  sphere lies at the lower detection bound for our experimental setup.

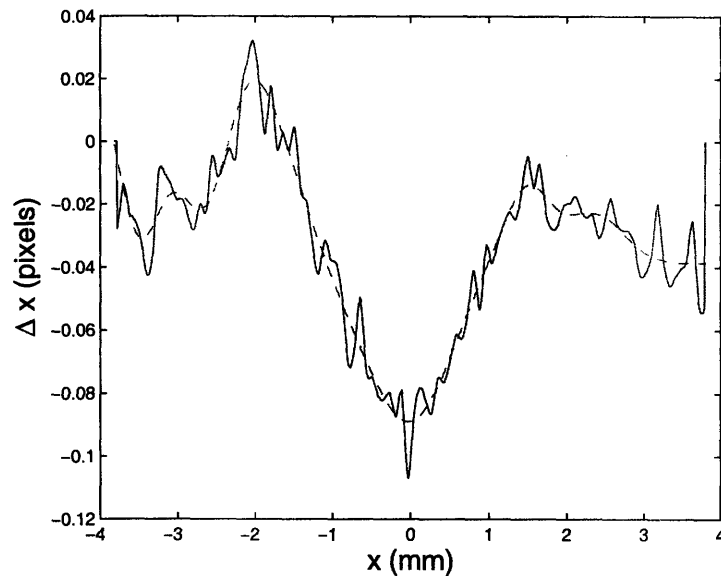


Figure 2-9: Apparent horizontal displacements of the mask for a  $157\ \mu\text{m}$  sphere.

To quantify the background noise we performed experiments in the absence of a settling sphere. A stratification was established and left to stand for six hours, after which apparent displacements of the mask were determined using the same technique as above. The noise, likely due to a combination of small-scale mechanical vibrations, light intensity fluctuations and thermal disturbances both external and internal to the microscope, was on the order of 0.02 pixels. This is at the limit of what can be detected using pattern-matching techniques [10].

At the other end of the scale, for strong density gradient distortions the Synthetic

Schlieren technique, which assumes small deflections of light rays, breaks down and is only capable of providing qualitative data. For a given sphere density, this effectively imposes an upper bound on the largest sphere whose wake can be studied quantitatively. Our experiments with a polystyrene sphere of 3.16 mm diameter, for example, produced mixing, which in turn generated highly nonlinear distortions of the mask.

## 2.4 Conclusion

In order to facilitate quantitative studies of environmental processes in the ocean involving the motion of microscale particles and organisms through stratified fluids, we have extended the application of Synthetic Schlieren techniques to the microscale. We tested our method on settling spheres, for which it is the structure of the wake rather than radiated internal waves that is primarily responsible for distorting the background stratification. In the wake, density gradient perturbations in the horizontal far exceed those in the vertical, requiring modification of the previous formulation of axisymmetric Synthetic Schlieren [29]. For quantitative data, the method is limited to axisymmetric disturbances, while it can still provide qualitative information on the flow structure for non-axisymmetric disturbances or in the presence of strong mixing.

We could clearly detect and characterize the wake of 780 and 383  $\mu\text{m}$  spheres, finding that lighter fluid is dragged downwards in a wake, the size of which greatly exceeds that of the sphere. As the sphere size was decreased further, the signal generated by the density gradient perturbations approached the background noise level. Even for a 157  $\mu\text{m}$  sphere, however, we were able to detect a wake signature. In Chapter 4 and 5 we will discuss the application of this technique to elucidate the fluid mechanics of a stratified wake, in particular the suggested strong increase in drag coefficient [43].





# Chapter 3

## Methods of Investigation

In this chapter, we provide the formulation of stratified drag coefficient. We present our methods of investigations, including drag measurement by time-lapse photography, wake visualization by microscale synthetic schlieren, and numerical methods. The results of numerical simulations were provided by Dr. Carlos Torres, and I performed the data analysis of the numerical simulations. Here we provide a brief overview of the numerical simulations for convenience, which also serves the purpose of comparing the experimental and numerical results.

### 3.1 Formulation of Stratified Drag Coefficient

The drag force  $F_D$  on a sphere in a homogeneous fluid can be written as

$$F_D = -6\pi\mu aU - \frac{\rho V}{2} \frac{dU}{dt} - 6a^2\rho\sqrt{\pi\nu} \int_{-\infty}^t \left( \frac{dU}{dt} \right)_{t=s} \frac{ds}{\sqrt{t-s}}, \quad (3.1)$$

where  $V$  is the volume of the sphere,  $\rho$  the density of the fluid and  $\mu$  its dynamic viscosity. The first term on the right is the Stokes drag for steady settling at speed  $U$ , the second is the added mass drag, arising because an accelerating sphere spends energy in accelerating the surrounding fluid, and the third is the Basset history drag, due to diffusion of vorticity from an accelerating sphere as the boundary layer forms.

The latter two terms are negligible under steady conditions. To adopt a consistent formulation of  $F_D$  across all  $Re$ , it is customary to write  $F_D = C_D^H \frac{1}{2} \rho U^2 \pi a^2$ , where the homogeneous drag coefficient  $C_D^H$  is a function of  $Re$ . For  $Re \ll 1$ ,  $C_D^H = 12/Re$ . While the latter relation is somewhat misleading, since  $F_D$  is independent of  $Re$  in this regime, empirical extensions of this formulation prove useful to bridge the small and moderate  $Re$  regimes. A widely used empirical relation is

$$C_D^H = \frac{12}{Re} + \frac{6}{1 + \sqrt{2Re}} + 0.4, \quad (3.2)$$

which holds for  $0 < Re < 2 \times 10^5$  with less than 10% error [50].

The problem of a sphere settling in a linearly stratified fluid is illustrated in figure 3-1(a). Adopting the formalism for a homogeneous fluid, under quasi-steady conditions (defined below) we write the drag force in a stratified fluid as  $F_D = C_D^S \frac{1}{2} \rho U^2 \pi a^2$ , where the unknown stratified drag coefficient  $C_D^S$  captures the influence of stratification. For a given stratifying agent, we expect  $C_D^S$  to depend on  $Re$  and  $Fr$ . In general,  $C_D^S$  will also depend on the Prandtl number  $Pr = \nu/D$ , where  $D$  is the diffusivity of the stratifying agent. Here we focus on salt stratifications ( $Pr = 700$ ) and briefly address temperature stratifications ( $Pr = 7$ ).

Settling in a stratified fluid is an inherently unsteady process, because the density contrast between particle and surrounding fluid, hence the particle speed, decreases during settling: eventually the particle comes to rest at its depth of neutral buoyancy. We will see, however, that settling is quasi-steady for the parameter regime explored here, as added mass and Basset terms are negligible. Then,  $U$  is set by the balance of drag and buoyancy forces:

$$C_D^S \frac{1}{2} \rho U^2 \pi a^2 = \frac{4}{3} \pi a^3 \Delta \rho g, \quad (3.3)$$

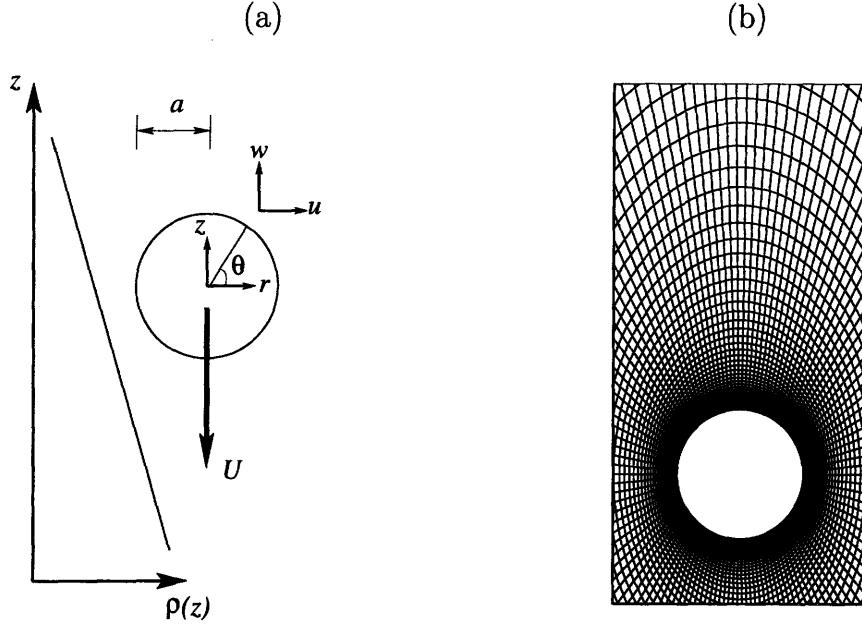


Figure 3-1: (a) Schematic of a sphere settling in a linearly stratified fluid. (b) The numerical grid in the region close to the sphere.

where  $\Delta\rho = \rho_P - \rho$  is the density contrast and  $\rho_P$  the particle density. This yields

$$C_D^S = \frac{8ga}{3U^2} \frac{\Delta\rho}{\rho}, \quad (3.4)$$

which enables  $C_D^S$  to be determined from measurements of  $\rho(z)$  and  $U(z)$ . To highlight the effect of stratification, one can normalize  $C_D^S$  by the locally homogeneous drag coefficient  $C_D^H$  from equation (3.2), here representing the drag coefficient the sphere would have if the entire water column had the density and viscosity of the fluid at that depth. The normalized drag coefficient

$$C_D^N = \frac{C_D^S}{C_D^H}, \quad (3.5)$$

reveals whether stratification does ( $C_D^N \neq 1$ ) or does not ( $C_D^N = 1$ ) affect drag.

## 3.2 Methods

To investigate the problem of a sphere settling in a linearly stratified fluid, we used a combination of time-lapse photography experiments to measure the stratified drag coefficient, visualization of the wake structure by microscale Synthetic Schlieren [51], and numerical simulations. Here we describe each approach.

### 3.2.1 Drag Measurement by Time-Lapse Photography

Experiments were performed in a 30 cm high, 51 cm long and 26 cm wide plexiglas tank, with 0.54 cm thick walls. The tank was covered with a lid to eliminate convection in the fluid due to evaporation. An initial set of experiments was performed in homogeneous salt-water solutions of densities 1000, 1019 and 1035 kg m<sup>-3</sup>, measured with an Anton-Parr DMA38 densitometer. For all other experiments, the tank was filled with linearly stratified salt water using a double-bucket system [30], and left to stand for at least five hours to dissipate any residual flows. To achieve larger density gradients, in some experiments the tank was first partially filled with fresh water, followed by linearly stratified salt water up to a density  $\rho_S$ , and finally with homogeneous salt water of density  $\rho_S$ .

Spherical density floats (American Density Floats) with densities ranging from 1010.0 to 1130.0 kg m<sup>-3</sup> in intervals of 10.0 kg m<sup>-3</sup> were released into the tank to measure  $d\rho/dz$ . Regular vertical spacing of the floats confirmed the linearity of the density profile  $\rho(z)$ . The density gradient was determined from a linear fit to  $\rho(z)$  and used to compute  $N$ , taking  $\rho_0 = 1000$  kg m<sup>-3</sup>. The small size of the floats (diameter = 7 mm) and their location far from the settling path ( $> 20$  cm) ensured they did not affect the density field. There was no discernible motion of the floats, demonstrating the absence of any convection in the tank.

Polystyrene spheres of radius  $a = 196$  and  $390$   $\mu\text{m}$  (Duke Scientific; coefficient of variation for  $a$ : 3% ) and density  $\rho_P = 1050$  kg m<sup>-3</sup> were used in the experiments. To

ensure the accuracy of  $\rho_P$ , we confirmed that the polystyrene spheres and the 1050  $\text{kg m}^{-3}$  density float came to rest at the same depth. We measured the temperature of the fluid at the depth of each observation by a needle thermometer located far from the settling path. The temperature and the corresponding density were used to calculate the local dynamic viscosity  $\mu$  [16], including the effect of salinity on viscosity. Before release, particles were mixed with a small amount of fluid from the surface of the tank and a minimal amount of soap as a wetting agent to prevent sticking. To ensure settling through the observation window, a single particle was released using a 1 ml pipettor through a partially submerged conical injector (a 1 ml pipette with its tip cut off) inserted in a 7 mm wide hole in the lid.

To avoid wall effects, the settling path was more than 5 cm ( $> 125a$ ) from the nearest wall of the tank, which corresponds to a less than 1% change in drag coefficient for a homogeneous fluid [8]. The spheres settled in front of a black background and were illuminated by a fiber-optic light source. A ruler placed to the side of the settling path, and at the same distance from the camera, was used to calibrate vertical distances, and set vertical by use of a plumb line. Images were captured over a 3 cm tall observation window at 3 to 12 frames/s using a JAI CV-M4+CL CCD camera controlled by DigiFlow [11] and spheres were subsequently tracked with Matlab (The Mathworks, Natick, MA). A particle appeared as a light spot on a dark background, and the centre of the spot was taken as the position of the particle. The time series of vertical position was smoothed by a three-point moving average, before computing the particle velocity  $U(z)$  using a four-point centre-difference approach [9].

For each experiment, characterized by a given combination of  $N$ ,  $a$  and  $\Delta\rho$ , ten replicate runs were performed to reduce errors associated with such factors as variability in particle size and injection conditions. At each vertical location, the mean velocity was computed as the average over these ten runs, as shown in figure 3-2(a). The mean velocity profile, in combination with  $\rho(z)$ , determined  $Re$ ,  $Fr$ ,  $Ri = Re/Fr^2$ , and  $C_D^N$ , which all varied over the vertical length of the observation window since

$\rho(z)$  increased with depth. Experiments were repeated for  $0.01 \leq Re \leq 1.57$  and  $0.09 \leq Fr \leq 6.75$  (figure 3-2(b)) by varying  $N$  and  $a$ . As a validation of our averaging procedure, two sets of ten runs were performed in two adjacent observation windows along the settling path, for  $a = 196 \mu\text{m}$  and  $N = 1.69 \text{ s}^{-1}$ . The two resulting curves in  $(Re, Fr^{-1})$  space (curves 1 and 2 in figure 3-2(b)) are a smooth continuation of each other. For all the settling experiments performed, calculation of  $dU/dt$  showed that the added mass and Basset force terms (equation 3.1) contributed less than 1% of the total drag force, justifying our earlier assumption of quasi-steady settling.

### 3.2.2 Wake Visualization by Microscale Synthetic Schlieren

To visualize the effect of the settling sphere on the fluid density field, we performed experiments using Microscale Synthetic Schlieren [51], as is presented in Chapter 2. Our experiments were performed in a 48 cm high, 6.3 cm long and 2.5 cm wide plexiglas tank, with 0.54 cm thick walls. The distance between the settling path and the closest wall ( $> 32a$ ) corresponded to a less than 5% change in drag coefficient for a homogeneous fluid [8]: as will be seen below, this is negligible compared to the effect of stratification.

Two forms of processing were used. The first, known as qualitative Synthetic Schlieren, consists simply in subtracting the reference image from each subsequent image and provides a proxy for the relative magnitude of density perturbation gradients. The second, quantitative Synthetic Schlieren, uses cross-correlation algorithms to compute the apparent displacements of the mask and inverts them to obtain the associated gradients in density perturbation. Details of the processing are given in [51]. Radial density perturbation gradients  $\partial\rho'/\partial r$  were then integrated along  $r$  at a given vertical position  $z$ , and this was repeated for each of the 600 vertical positions (i.e. 600 vertical pixels) in an image, yielding the density perturbation field  $\rho'$ . This was added to the background density field, enabling calculation of isopycnals by con-

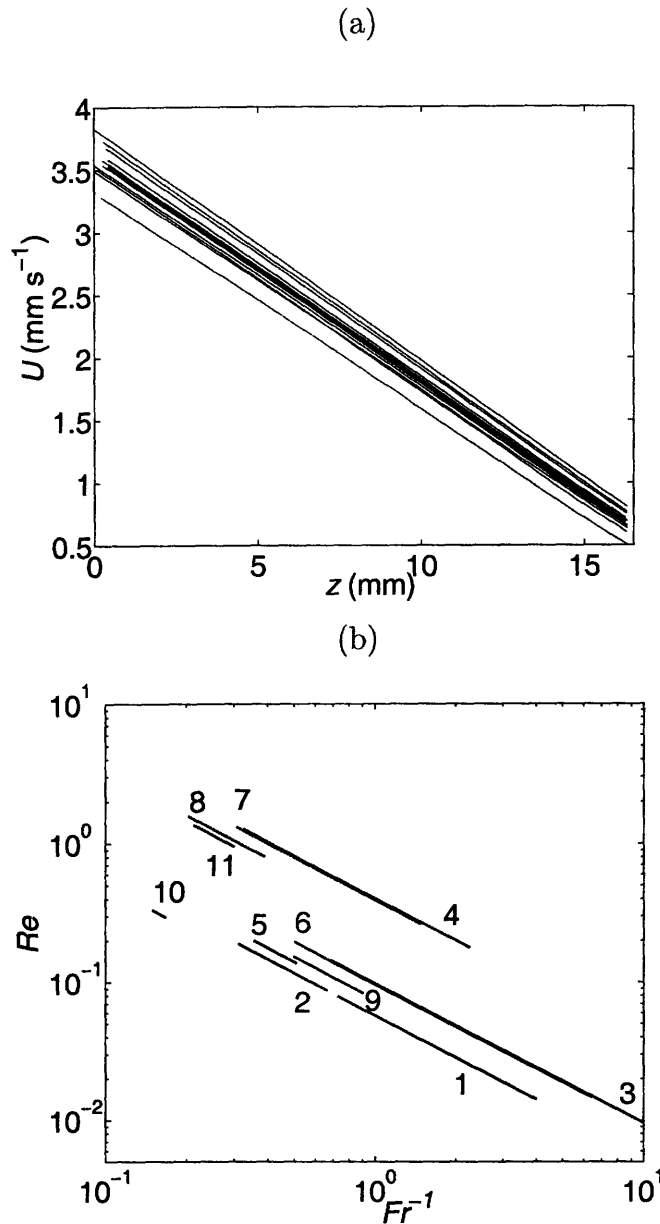


Figure 3-2: (a) The settling velocity  $U$  versus depth  $z$  for ten replicate experiments (faint lines), along with the mean (bold line), for  $a = 390 \mu\text{m}$  and  $N = 2.92 \text{ s}^{-1}$ . (b) The parameter regime explored experimentally, shown in terms of  $Re$  and  $Fr^{-1}$ . Each experiment is represented by a continuous curve, because a particle samples decreasing  $Re$  and  $Fr$  as it settles into progressively denser fluid. Curves at larger  $Fr$  are shorter because in a weaker stratification  $U$  (and thus  $Re$  and  $Fr$ ) varies less over a given vertical window. All experiments were conducted at  $Pr = 700$  (salt stratification). Two sphere sizes were used:  $a = 196 \mu\text{m}$  (experiments 1,2,3,5,6,9,10) and  $a = 390 \mu\text{m}$  (experiments 4,7,8,11).

touring the total density field in Matlab.

### 3.2.3 Numerical Model

Numerical simulations were performed for comparison of the drag coefficient with experimental data and to obtain high resolution information on the density and flow fields over a wide range of parameters. Simulations were carried out in the parameter regime  $0.05 \leq Re \leq 2.1$ ,  $0.02 \leq Fr \leq 200$ , and  $7 \leq Pr \leq 700$ . The model was adapted from an earlier one [43, 23] and is described here only briefly. It considers flow of a linearly stratified fluid at constant velocity  $U$  past a stationary sphere (figure 3-1(a)), and uses finite-differences to solve the nondimensional equations

$$\frac{\partial \mathbf{u}}{\partial t} + \mathbf{u} \cdot \nabla \mathbf{u} = -\nabla p - \frac{\rho'}{Fr^2} \mathbf{j} + \frac{1}{Re} \nabla^2 \mathbf{u}, \quad (3.6)$$

$$\frac{\partial \rho'}{\partial t} + \mathbf{u} \cdot \nabla \rho' = w - 1 + \frac{1}{RePr} \nabla^2 \rho', \quad (3.7)$$

$$\nabla^2 p = -\frac{1}{Fr^2} \nabla \cdot (\rho' \mathbf{j}) - \nabla \cdot [(\mathbf{u} \cdot \nabla) \mathbf{u}] + \frac{1}{Re} \nabla^2 P - \frac{\partial P}{\partial t}, \quad (3.8)$$

obtained by rescaling lengths by  $a$ , velocities by  $U$ , pressure perturbations by  $\rho_0 U^2$ , and density perturbations by  $-a (d\rho/dz)$ . Here  $\mathbf{u} = (u, w)$  is the fluid velocity in the radial and vertical direction, respectively,  $p$  the pressure,  $\mathbf{j}$  the vertical unit vector, positive upwards, and  $P = \nabla \cdot \mathbf{u}$ . Equation (3.8) replaces the incompressibility condition: when discretizing  $\partial P/\partial t$  as  $(P^{n+1} - P^n)/\Delta t$  ( $n$  refers to the integration time  $t = n\Delta t$  and  $\Delta t$  is the integration step), incompressibility was enforced by setting  $P^{n+1} = 0$ . The boundary conditions on the surface of the sphere were  $\mathbf{u} = 0$  and zero density flux, enforced by requiring  $(\partial \rho'/\partial z) z + (\partial \rho'/\partial r) r = z$ . The surface boundary condition for pressure was obtained from equation (3.6) by setting  $\mathbf{u} = 0$ . Far from the sphere, all physical quantities tended to their unperturbed values:  $\mathbf{u} = (0, 1)$  at the upstream (lower) boundary,  $\partial \mathbf{u}/\partial z = 0$  at the downstream (upper) boundary,



and  $\rho' = 0$ ,  $\partial p / \partial n = 0$  at both.

To improve accuracy near the sphere surface while simplifying the implementation of boundary conditions, equations (3.6)–(3.8) were written in curvilinear coordinates  $(\xi, \eta)$  and solved on a curvilinear grid (figure 3-1(b)), as described in [43]. The external boundary of the grid was elliptic, with axes lengths of 80 (vertical) and 40 (horizontal). The grid consisted of  $65 \times 91$  or  $195 \times 91$  ( $\xi \times \eta$ ) mesh points, non-uniformly distributed with a higher mesh density near the sphere and a smallest grid size of  $8.2 \times 10^{-4}$ . The grid ensured that the density boundary layer  $\delta_\rho = O((Re Pr)^{-1/2})$  was accurately resolved: for  $Pr = 700$  and  $Re = 1$ ,  $\delta_\rho = 0.038$  was covered by 16 grid points. This also ensured resolution of the momentum boundary layer, which was always thicker than the density boundary layer since  $Pr > 1$ .

For the small Reynolds number stratified regime investigated here, the GMRES (Generalized Minimal RESidual method) was found to be superior in solving the Poisson equation for pressure (3.8) compared to the Successive Overrelaxation Method [23] used in a previous version of the code [43]. The solution procedure was then as follows: given  $\mathbf{u}$  and  $\rho$  at time  $t = n \Delta t$ ,  $p$  was obtained from equation (3.8) using GMRES and substituted into equations (3.6) and (3.7). Solution of the latter two equations yielded updated values of  $\mathbf{u}$  and  $\rho$  at  $t = (n + 1) \Delta t$ . Equations (3.6)–(3.8) constitute a time-dependent problem, but here we were interested in steady solutions. Therefore, the cycle was repeated starting from  $\mathbf{u} = (0, 1)$ ,  $\rho' = 0$  until the convergence criterion  $|f^{n+1} - f^n|_{max} < 10^{-4}$  was satisfied, where  $f$  represents any one of  $u$ ,  $w$ ,  $p$  or  $\rho$ . The time step was  $\Delta t = 0.0025$  or  $0.0001$  and steady state was typically reached within  $t = 30$ . Extensive convergence tests on time step and mesh size were carried out by Larrazbal *et al.*[23].

The drag coefficient  $C_D^S$  was computed as the sum of the pressure ( $C_P^S$ ) and viscous ( $C_V^S$ ) drag coefficients:

$$C_P^S = -\frac{1}{\frac{1}{2}\rho U^2 \pi a^2} \int_S p \mathbf{n} \cdot \mathbf{j} dS, \quad (3.9)$$

$$C_V^S = \frac{1}{\frac{1}{2}\rho U^2 \pi a^2} \int_S \mu \mathbf{n} \cdot ((\nabla \mathbf{u}) + (\nabla \mathbf{u})^T) \cdot \mathbf{j} dS, \quad (3.10)$$

where  $\mathbf{n}$  is the unit vector normal to the sphere surface  $S$ , positive outward. Drag coefficients were normalized by their homogeneous counterparts to obtain the normalized drag coefficients  $C_D^N$ ,  $C_P^N$  and  $C_V^N$ .

# Chapter 4

## Results and Discussion

In this chapter we provide the results of experiments and numerical simulations. We discuss the origin of enhanced drag and present a scaling argument to rationalize the stratified drag coefficient law. We elucidate a physical mechanism responsible for the enhanced drag in a stratified fluid at low  $Re$ , which is drastically different from mechanisms proposed at higher  $Re$ .

### 4.1 The drag due to stratification

We begin by reporting experimental results for particles released in homogeneous salt-water solutions. Unless otherwise noted, all results are expressed in dimensionless form as described in section 3.3. Using the measured terminal settling velocity  $U$ ,  $C_D^H$  was computed from a balance of buoyancy and drag (equation 3.4, for  $C_D^H$  instead of  $C_D^S$ ). This was repeated for four fluid densities. Results are reported as a function of  $Re$  in figure 4-1 and compared to the prediction from equation (3.2). The good agreement validates our procedure for measuring settling velocity, ensuring that drag coefficients can be reliably determined. A validation of the numerical model was performed by computing  $C_D^S$  for various  $Re$  and  $Fr = 200$ . At this high value of  $Fr$ , stratification is unimportant and as one would expect the calculated values of  $C_D^S$  tend to  $C_D^H$  (figure 4-1).

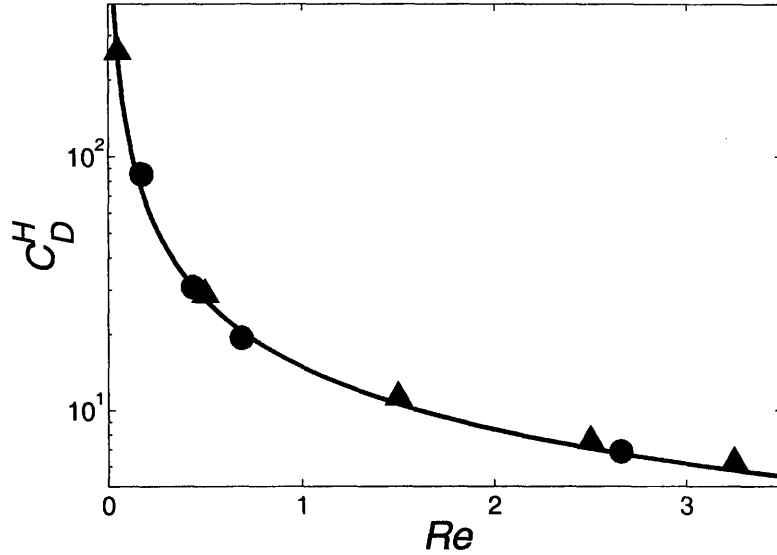


Figure 4-1: The homogeneous drag coefficient  $C_D^H$  measured experimentally (circles) and computed numerically (triangles), compared with the prediction from equation (3.2) (continuous line), as a function of  $Re$ .

We proceeded to measure drag in a linearly stratified fluid and present results in terms of the normalized drag coefficient  $C_D^N$ . This is shown as a function of  $Fr^{-1}$  and  $Ri$  in figures 4-2(a,b), respectively. The choice of  $Fr^{-1}$  as the independent parameter is appropriate at moderate  $Re$  [43, 19], while  $Ri$  is suggested by the theoretical analysis of Zvirin and Chadwick [53]. Three important conclusions emerge. The first is that  $C_D^N > 1$ , demonstrating that a linear stratification does increase drag at small  $Re$ ; indeed, our experiments reveal that stratified drag can be more than three-fold greater than its homogeneous counterpart. Secondly,  $C_D^N$  increases monotonically with both  $Fr^{-1}$  and  $Ri$ , showing that stronger stratifications result in larger drag. Thirdly, the data collapses considerably better when plotted against  $Ri$  than against  $Fr^{-1}$ , implying that  $Re$  and  $Fr$  affect  $C_D^N$  only through the combination  $Ri = Re/Fr^2$  at small  $Re$ . We found a fit of the form  $1 + \alpha Ri^q$  appropriate to describe the dependence of  $C_D^N$  on  $Ri$ , with the best fit for the experiments given by  $C_D^N = 1 + 1.95 Ri^{0.62}$ .

Drag coefficients were also computed numerically. We performed two sets of simulations ( $Re = 0.05$  and  $0.5$ ) at  $Pr = 700$  to model a salt stratification (the data set for

$Pr = 7$  represents a temperature stratification and will be discussed later). Numerical results (figure 4-2) confirm that  $C_D^N > 1$  and there is good quantitative agreement with the experiments. Furthermore, numerical results likewise reveal the clear dependence of  $C_D^N$  on  $Ri$  by successfully collapsing data for two different  $Re$ . A best fit to the combined numerical data for  $Re = 0.05$  and  $0.5$  yields  $C_D^N = 1 + 1.91 Ri^{0.41}$  ( $C_D^N - 1 \sim Ri^{0.39}$  for  $Re = 0.05$ ;  $C_D^N - 1 \sim Ri^{0.43}$  for  $Re = 0.5$ ). This is a slightly weaker dependence compared to the experiments, but the difference in  $C_D^N$  predicted from the two fits is  $< 15\%$  over the experimental parameter range.

Numerical results further reveal that both the pressure and viscous components of drag increase with  $Ri$  (figures 4-3(a,b)). For  $Ri = 0$ ,  $C_P^N = 1/3$  and  $C_V^N = 2/3$ , as expected for Stokes flow. The scaling of  $C_P^N - 1/3$  and  $C_V^N - 2/3$  with  $Ri$  is similar to  $C_D^N - 1$ , with a slightly larger exponent for  $C_P^N$ . To understand the origin of pressure and viscous drag increase, in figures 4-4(a,b) we plot the pressure and the vertical component of the tangential shear stress along the surface of the sphere, respectively, corresponding to the integrands in equations (3.9)–(3.10). An increase in  $Ri$  induces a larger front-aft pressure difference (figure 4-4(a)), resulting in increased pressure drag, and enhances shear stresses, particularly at the equator (figure 4-4(b)), accounting for the larger viscous drag.

To understand the origin of the increase in pressure and viscous drag, the drag force  $\mathbf{F}_D$  can be written as

$$\mathbf{F}_D = - \int_S p \mathbf{n} dS + \mu \int_{V_F} \nabla \wedge \boldsymbol{\omega} dV_F, \quad (4.1)$$

where  $S$  is the surface area of the sphere,  $V_F$  is the volume of the fluid domain,  $p$  is the pressure, and  $\boldsymbol{\omega} = \nabla \wedge \mathbf{u}$  is the vorticity. The two terms represent pressure and viscous drag, respectively. Numerical results can be used to study the changes in the vorticity fields with  $Ri$ . The effect of stratification on viscous drag can be examined by studying the vertical component of  $\nabla \wedge \boldsymbol{\omega}$ . Figures 4-5 (a) and (b) present this

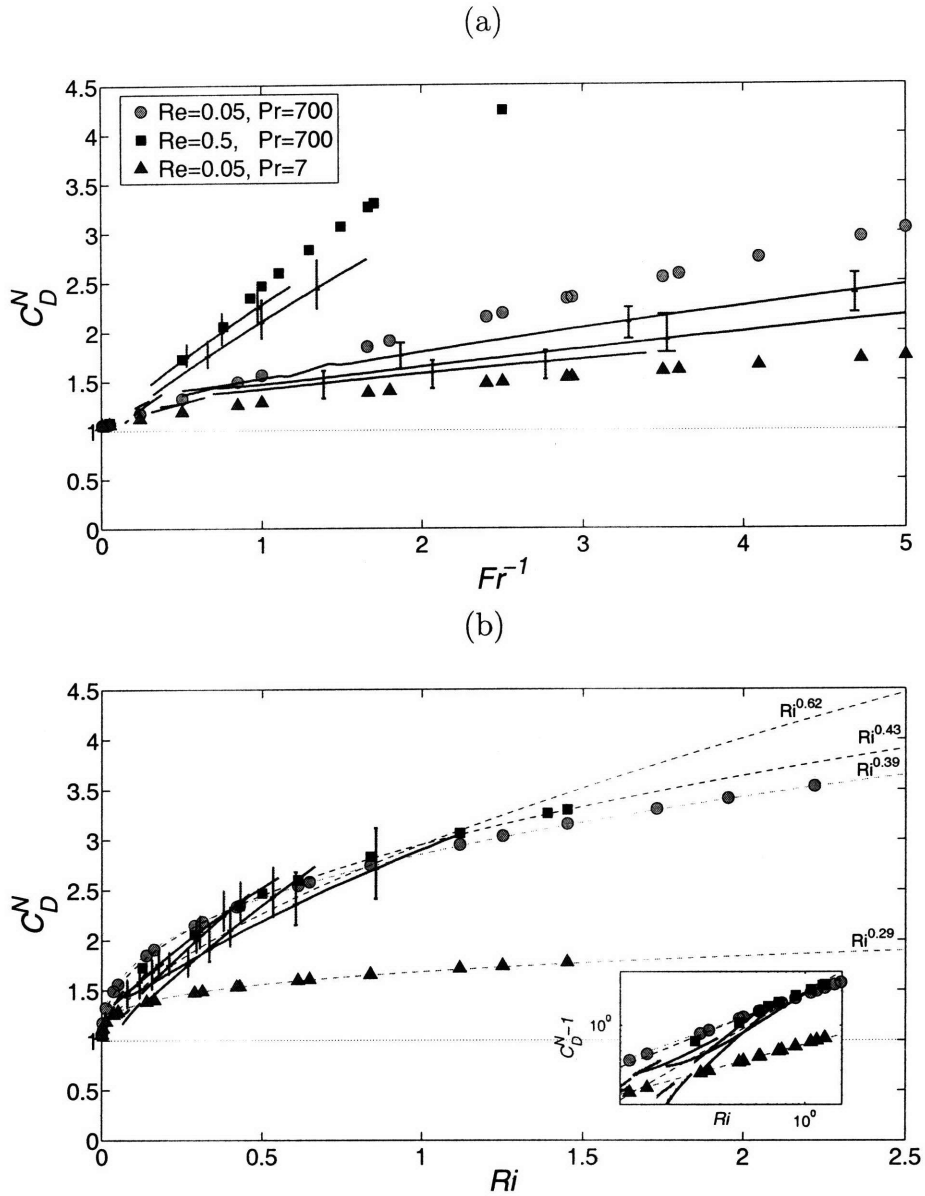


Figure 4-2: The normalized drag coefficient  $C_D^N$  as a function of  $Fr^{-1}$  for experiments (solid blue lines) and numerical simulations (symbols). The bars represent upper and lower bounds of experimental values. (b)  $C_D^N$  as a function of  $Ri$  for experiments (solid blue lines) and simulations (symbols). Dashed lines represent power law fits, performed separately for the experiments and each set of simulations, and color-coded accordingly. Inset: detail of  $C_D^N - 1$  vs.  $Ri$  in log-log scale.

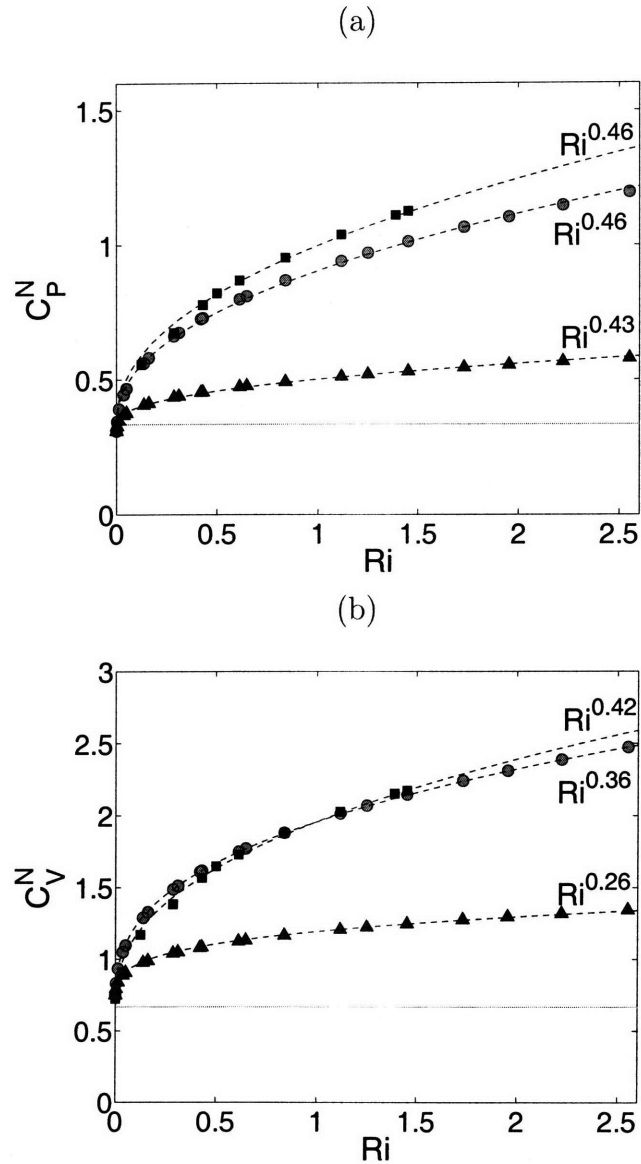


Figure 4-3: (a, b) The numerical pressure drag coefficient  $C_P^N$  and viscous drag coefficient  $C_V^N$  vs.  $Ri$ , along with best fit power laws (dashed lines). In all panels, dotted lines represent the theoretical prediction for homogeneous Stokes flow ( $Ri = 0$ ):  $C_D^N = 1$ ,  $C_P^N = 1/3$  and  $C_V^N = 2/3$ .

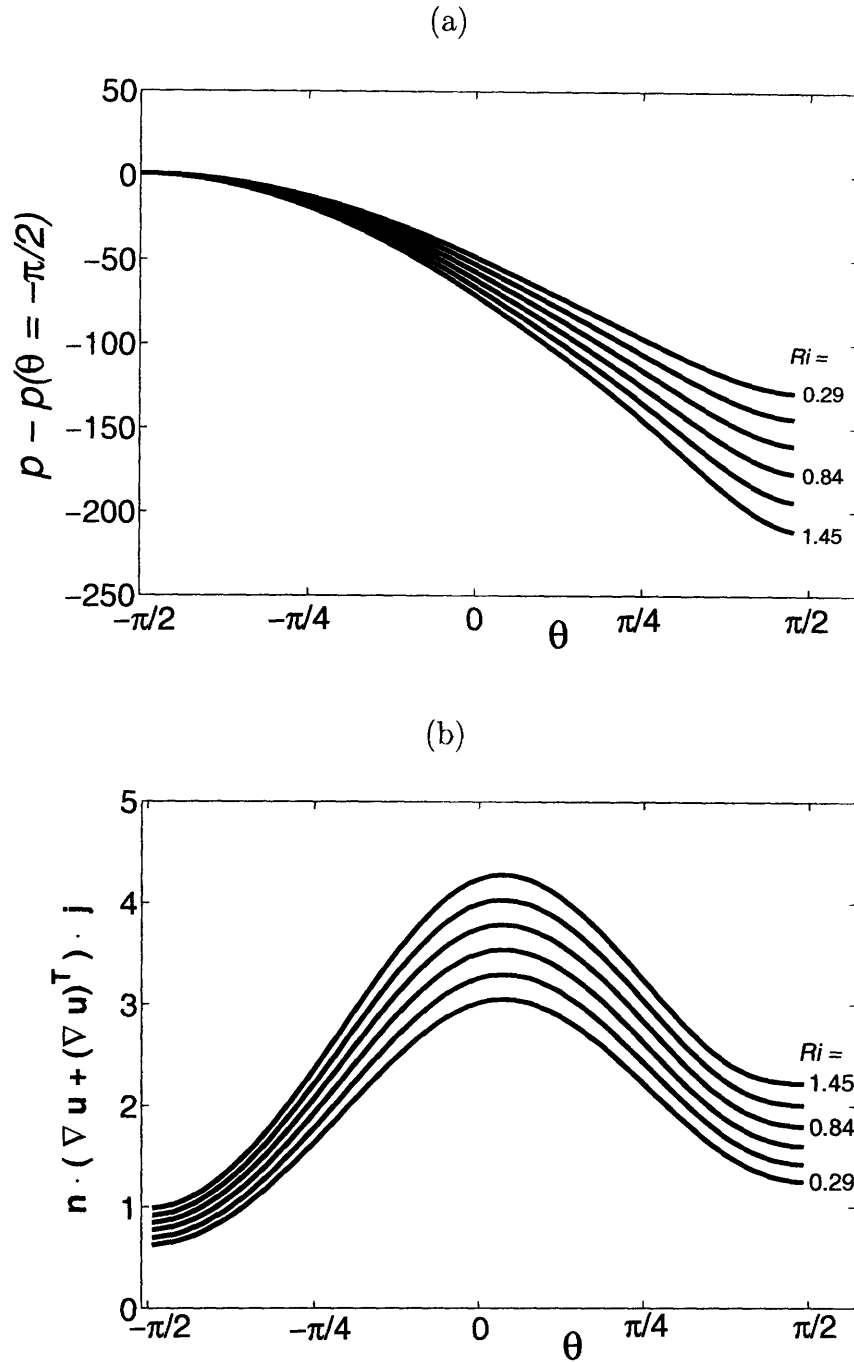


Figure 4-4: (a) Pressure and (b) vertical component of the tangential shear stress, along the surface of a settling sphere for  $Re = 0.05$  and different  $Ri$ .  $Ri = 0.29, 0.43, 0.61, 0.84, 1.12, 1.45$  from top to bottom in panel (a), and from bottom to top in panel (b).  $\theta = -\pi/2$  is the front of the sphere (figure 3-1).



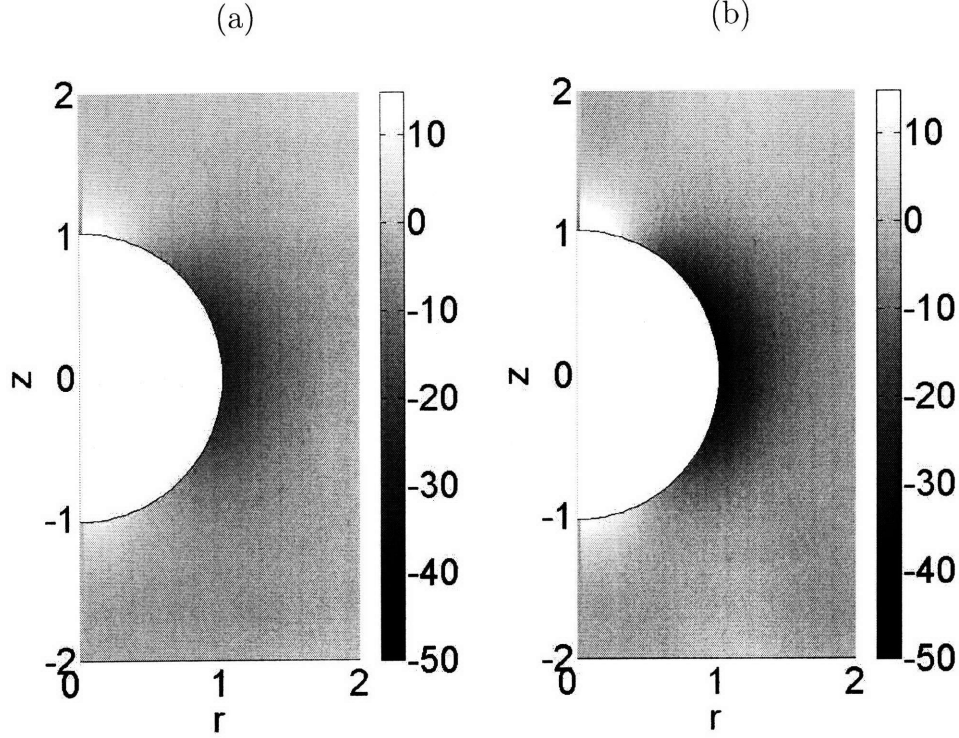


Figure 4-5: (a, b)  $(\nabla \wedge \omega) \cdot \mathbf{j}$  for (a)  $Ri = 0.29$  ( $Re = 0.05, Fr = 0.42$ ) and (b)  $Ri = 1.45$  ( $Re = 0.05, Fr = 0.19$ ). A stronger stratification results in a larger downward component of  $\nabla \wedge \omega$ , hence a large viscous drag.

data for  $Ri = 0.29$  and  $1.45$ , revealing that the vertical downward component of  $\nabla \wedge \omega$  increases with  $Ri$ , resulting in a larger viscous drag force. The signature of stratification is also apparent in the vorticity field itself. Figures 4-6 (a) and (b) show  $\omega$  for  $Ri = 1.25 \times 10^{-6}$  and  $1.45$ , respectively, while panel (c) shows a radial transect of  $\omega$  taken at the equator ( $z = 0$ ). When  $Ri \sim 0$ , we recover the front-aft symmetric distribution expected for homogeneous Stokes flow. For larger  $Ri$ , vorticity contours become asymmetric, with higher concentration near the rear of the sphere, squeezed towards the sphere's surface, and  $\omega$  at the surface increases significantly (note the different gray scales in panels (a) and (b)). This corresponds to higher velocity gradients near the rear of the sphere, higher viscous stresses, and hence a larger viscous drag force. Figures 4-6 (d) shows streamlines for  $Ri = 1.25 \times 10^{-6}$  and  $1.45$ , respectively. For larger  $Ri$ , streamlines become asymmetric.

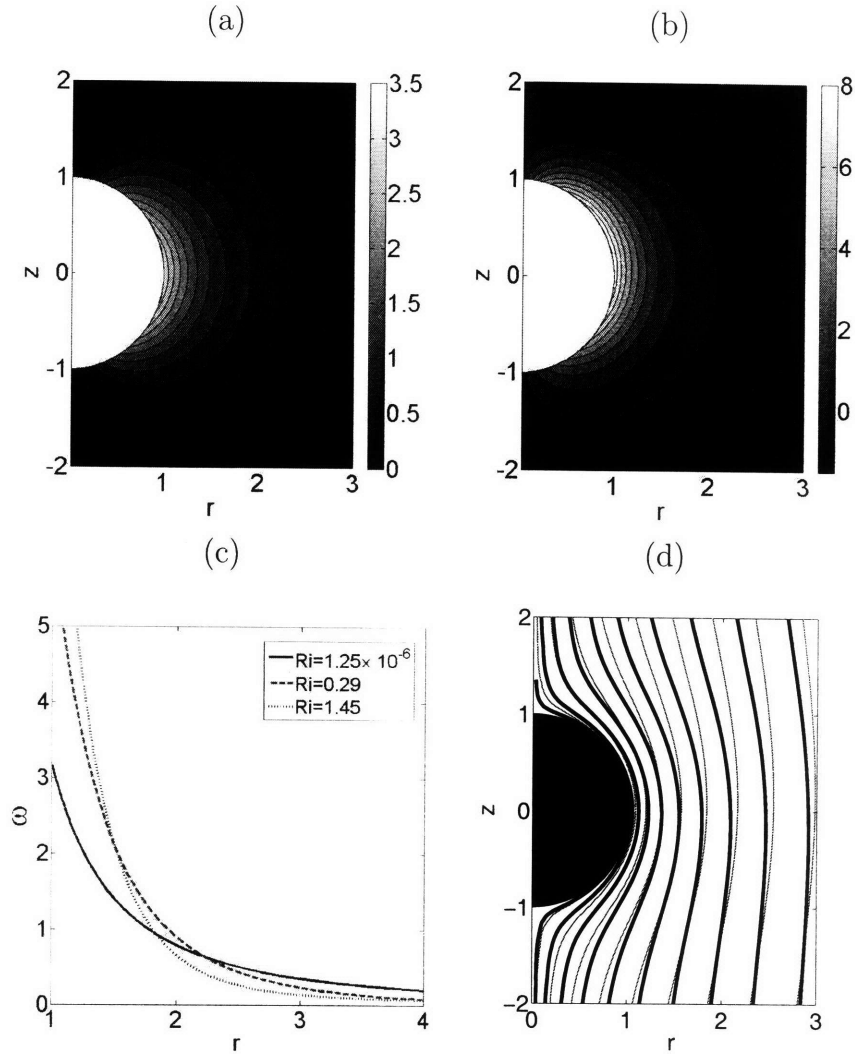


Figure 4-6: (a, b) Vorticity field  $\omega$  around the sphere for (a)  $Ri = 1.25 \times 10^{-6}$  ( $Re = 0.05$ ,  $Fr = 200$ ) and (b)  $Ri = 1.45$  ( $Re = 0.05$ ,  $Fr = 0.19$ ). (c) Radial distribution of vorticity at the equator of the sphere ( $\theta = 0$ ) for the same values of  $Ri$ . Vorticity is compressed towards the sphere and enhanced at higher  $Ri$ . (d) Streamlines around the sphere for  $Ri = 1.25 \times 10^{-6}$  (thin lines) and  $Ri = 1.45$  (thick lines)

## 4.2 The wake

Further detail on the nature of the wake behind a settling sphere was obtained using Microscale Synthetic Schlieren. Figure 2-4 shows a qualitative Synthetic Schlieren image for an  $a = 390 \mu\text{m}$  sphere settling in a stratification with  $N = 1.31 \text{ s}^{-1}$  (corresponding to  $Re = 2.1$ ,  $Fr = 10.2$ ,  $Ri = 0.02$ ). As described by Yick *et al.* [51], due to the limited depth of focus of the microscope, the position of the sphere is known to within one sphere radius. Several features of the wake are immediately apparent. It is symmetric about the central axis, as one would expect from radial symmetry, and is of considerable length ( $> 22 \text{ mm}$ ), revealing that the stratification remains perturbed far downstream of the sphere. The wake structure becomes more complex near its end, in the form of a pair of faint white lobes.

Quantitative processing of this data yields the density field in the wake of the sphere (figure 4-7(a)). Isopycnals are dragged down by as much as five sphere radii. Vertical isopycnal displacement diminishes with distance  $z$  downstream of the sphere, as isopycnals return to their neutral buoyancy position. As the viscous force resisting this retreat decreases with both  $z$  and  $r$ , retreating isopycnals overshoot on the rim of the wake at  $z \sim 20$ , creating a toroidal structure akin to that of a laminar buoyant jet [41]. This mild overshoot, which is responsible for the white lobes in figure 2-4, is locally damped by viscosity and does not trigger internal waves.

Several key features of the wake are confirmed by the numerical density field, shown in figure 4-7(b). The wake length is similar for experiments and numerics, and in both cases isopycnals overshoot without radiating internal waves. The deformation of numerical isopycnals is somewhat sharper compared to experiments, for reasons that we could not determine. Several possibilities were tested and discounted, including the resolution of the camera, random dot pattern, Schlieren processing and numerical grid. It is interesting, however, that drag coefficients are in good agreement (figure 4-2). Added drag will later be rationalized in terms of the buoyancy of

fluid in the immediate vicinity of the sphere. In this region, isopycnal distortion in experiments and numerics is comparable.

Taking a closer look at the numerical results in the vicinity of the sphere, we see that isopycnals are strongly compressed in front of the sphere (figure 4-8(a)), resulting in an increased pressure gradient (figure 4-4(a)) and hence pressure drag (figure 4-2(c)). As the sphere descends, isopycnals make way and tilt (figure 4-8(b)), causing baroclinic generation of vorticity, which enhances shear stresses (figure 4-4(b)) and thus viscous drag (figure 4-2(d)). This can be understood by considering the vorticity transport equation:

$$\frac{D\omega}{Dt} = \nu \nabla^2 \omega + \frac{\nabla p \wedge \nabla \rho}{\rho^2}, \quad (4.2)$$

where vortex stretching ( $\omega \cdot \nabla \mathbf{u}$ ) has been neglected because of axisymmetry. Except for diffusion, vorticity varies only due to tilting of isopycnals relative to isobars: this tilting increases the vorticity of the fluid as it travels past the sphere. At the rear, isopycnals detach from the sphere, however without generating the buoyant jet (figure 4-8(c)) characteristic of higher  $Re$  [43]. On the larger scale, simulations predict that wake length and isopycnal deflection decrease with increasing  $Ri$  (figure 4-9), since enhanced buoyancy more effectively opposes vertical motion and more rapidly restores isopycnals. These features of the numerical solution are supported by further experimental observations. As shown in figure 4-10(a), the only region where Synthetic Schlieren detected vertical pattern displacements (corresponding to vertical density gradients) was ahead of the sphere, in contrast to the strong horizontal pattern displacements that were detected in the wake (figure 4-10(b)). Furthermore, the length of the wake and the magnitude of isopycnal distortion both clearly diminished as  $Ri$  increased (figure 4-10(b,c)).

### 4.3 Discussion

The primary result of this study is that stratification increases hydrodynamic drag on a sphere settling at small  $Re$ : both experiments and numerical simulations re-

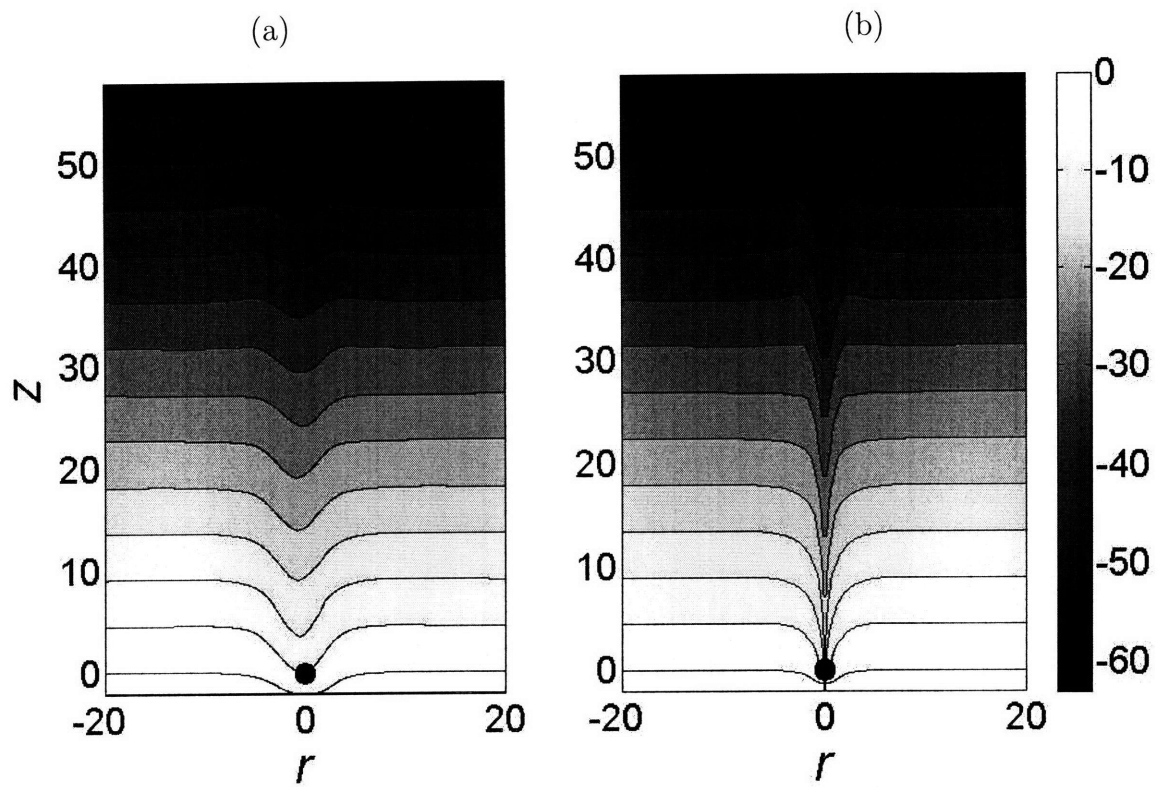


Figure 4-7: Dimensionless density field  $\rho - \rho(0)$  in the wake of a settling sphere for  $Ri = 0.02$  ( $Re = 2.1, Fr = 10.2$ ) obtained from (a) Microscale Synthetic Schlieren and (b) numerical simulation.

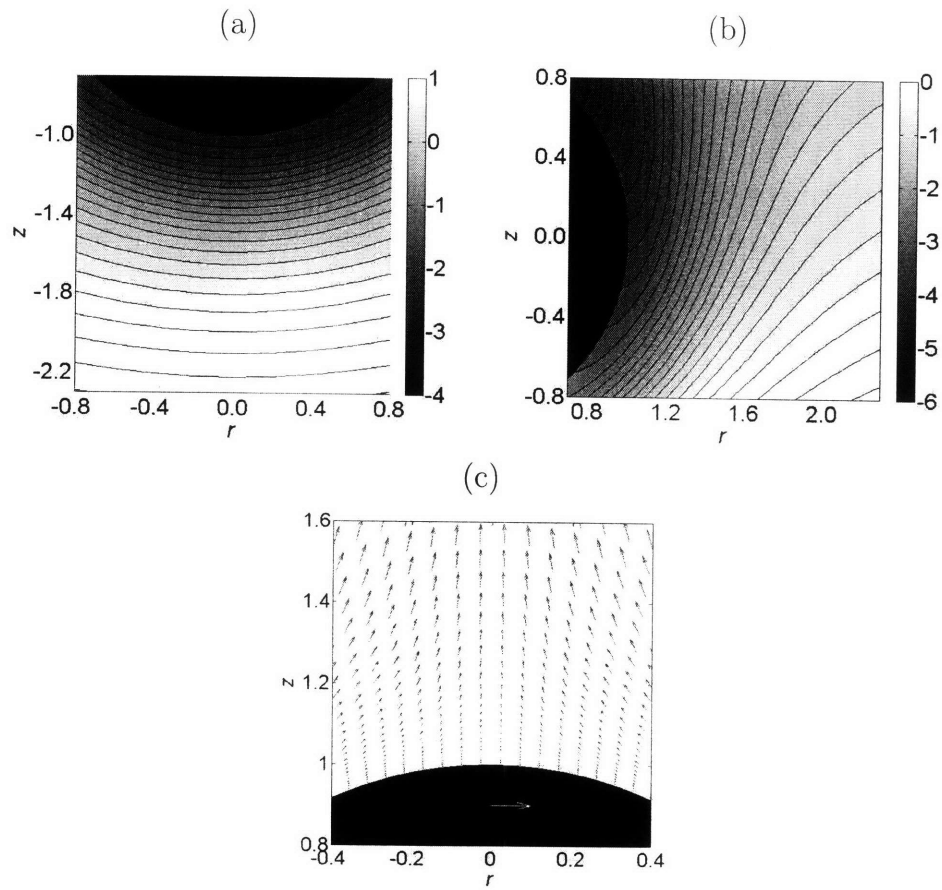


Figure 4-8: (a, b) Numerical isopycnal distortion at two locations around the sphere. Colorbars show  $\rho - \rho(0)$ . (c) Numerical velocity field behind the sphere. For all cases,  $Ri = 0.29$  ( $Re = 0.05$ ,  $Fr = 0.42$ ).

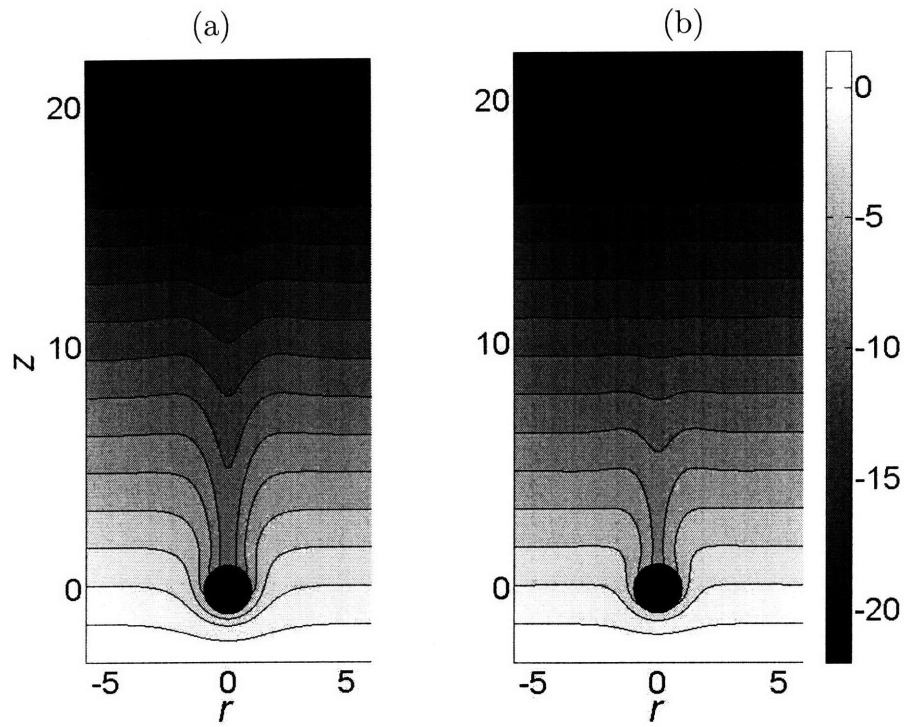


Figure 4-9: Numerical density field  $\rho - \rho(0)$  in the wake of a settling sphere for (a)  $Ri = 0.29$  ( $Re = 0.05, Fr = 0.42$ ) and (b)  $Ri = 1.45$  ( $Re = 0.05, Fr = 0.19$ ). Higher  $Ri$  corresponds to a shorter wake and smaller isopycnal deflections.

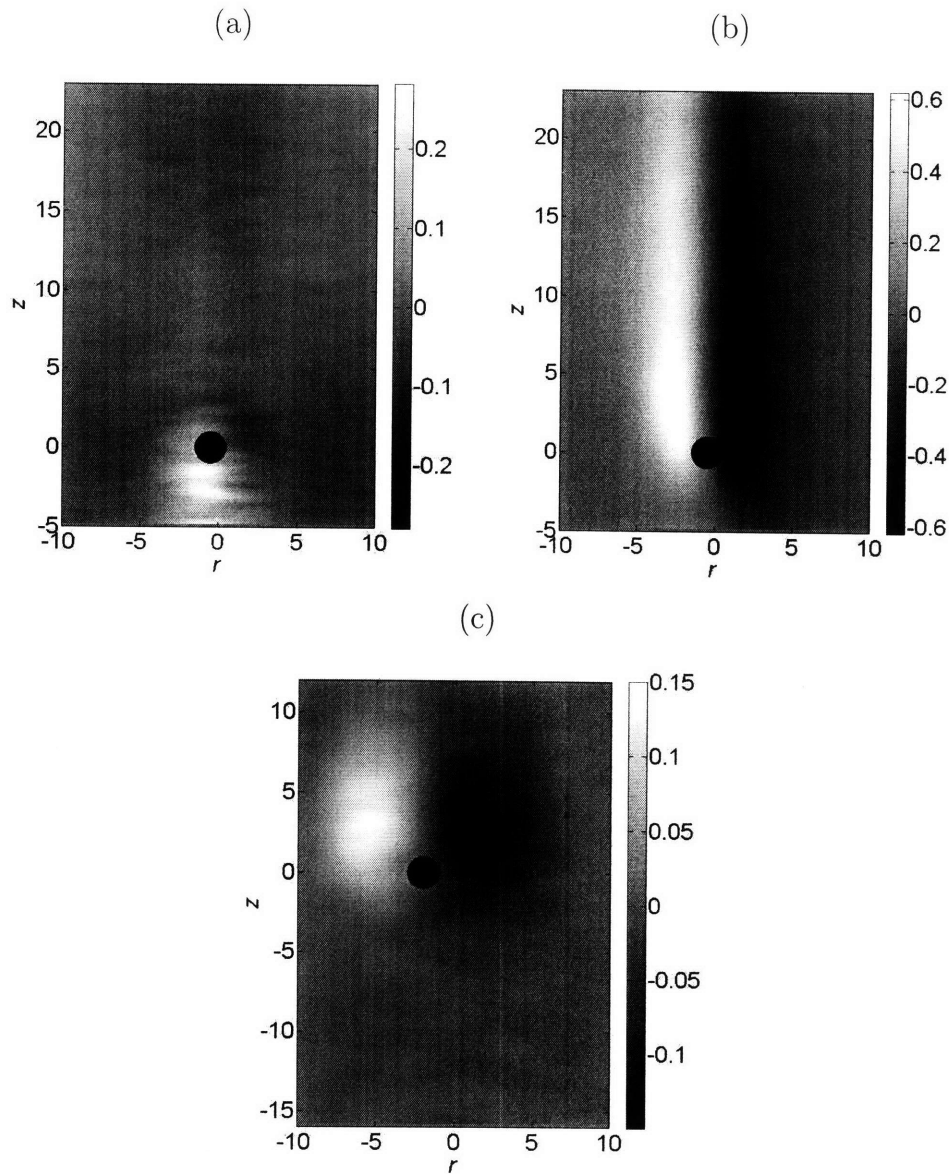


Figure 4-10: (a) Horizontal and (b,c) vertical pattern displacements generated by an  $a = 390 \mu\text{m}$  settling sphere, detected using Microscale Synthetic Schlieren. Colorbar units are in pixels. (a,b)  $N = 1.31 \text{ s}^{-1}$  ( $Ri = 0.02, Re = 2.1, Fr = 10.2$ ); (c)  $N = 2.50 \text{ s}^{-1}$  ( $Ri = 0.89, Re = 0.15, Fr = 0.4$ ). The position of the sphere, added in postprocessing, is accurate to within one sphere radius. Note the different colorbar scale in (b) and (c).



vealed that  $C_D^N > 1$ . For a given stratifying agent (i.e.  $Pr$ ), the drag increase is best characterized by  $Ri = Re/Fr^2$ . The latter arises naturally when considering the relative importance of buoyancy and viscous forces, which can be expressed as  $\int_{V_F} g \Delta\rho dV / \int_{S_F} \mu(\partial w/\partial r) dS$ , where  $V_F$  and  $S_F$  are the volume and surface area of a fluid element; assuming that lengths scale with  $a$ , speeds with  $U$  and density contrast with  $a$  ( $d\rho/dz$ ), this ratio scales like  $Ri$ . The experimentally and numerically determined drag coefficients are in good quantitative agreement (figure 4-2(b)), reaching up to 3.4 times the homogeneous value for  $0 < Ri < 2$ . To further increase  $Ri$  while maintaining  $Re$  small,  $N$  would have to be increased beyond our maximum value of  $2.92 \text{ s}^{-1}$ ; such large values are rare in nature. Considering both experimental and numerical results, our study suggests that the normalized drag coefficient scales as  $C_D^N - 1 \sim Ri^q$ , where  $q = 0.51 \pm 0.11$ , in contrast to the theoretical prediction  $q = 1/3$  for  $Ri \ll 1$  [53].

The observed added drag due to stratification at small  $Re$  complements earlier studies at higher  $Re$  [38, 43, 19] and it is worthwhile to assess whether previously proposed mechanisms can account for our findings. For a linear stratification at  $25 \leq Re \leq 100$ , Torres *et al.* [43] found that the increase in drag of a settling sphere was related to a rear buoyant jet; the current numerical studies, however, reveal no sign of such a jet (figure 4-8(c)), consistent with the increased importance of viscous forces, which prevent a rapid retreat of isopycnals. For a step-wise stratification at  $1.5 < Re < 15$ , Srdić-Mitrović *et al.* [38] found that the increased drag on a sphere was accounted for by the buoyancy in the entire wake of dragged-down fluid. In our case, integration of the buoyancy over the entire wake in figure 4-7(a) results in a force ( $13.0 \times 10^{-8} \text{ N}$ ) far larger than the measured increase in drag ( $1.5 \times 10^{-8} \text{ N}$ ). That drag does not depend on the entire wake is further supported by the numerical results in two manners. Firstly, two wakes can have significantly different size (figure 4-11), hence buoyancy, and yet the same drag coefficient (figure 4-2). Secondly, a force balance on the wake that ignores the contribution of the sphere yields a scaling argument that successfully predicts its width  $W$ . The balance between viscous and

buoyancy forces suggests  $(\mu U/W) W^2 \sim g \Delta \rho W^3$ , where  $\Delta \rho \sim N^2 \rho_0 W/g$  and vertical isopycnal deflections are assumed to also scale with  $W$ . This yields  $W/a \sim Ri^{-1/3}$ , which is borne out by the numerical results in figure 4-13, where  $W$  was taken as the distance from the axis of symmetry to the point where vertical isopycnal deflection decreased to  $0.1a$ .

### 4.3.1 Physical Mechanism for Added Drag

Instead, we propose that it is the buoyancy of a localized fluid region around the sphere that determines the added drag. This is related to the work by Higginson *et al.* [19] at higher  $Re$  ( $\sim O(10^3)$ ), where added drag on a rising grid of bars was found to derive from the buoyancy of fluid in the drift volume. In our case, the fluid volume affecting drag can be identified by considering the vertical velocity field  $w$  (figure 4-12(b)), which reveals that the wake is composed of two distinct regions: a lower one surrounds the sphere and descends at nearly its same speed ( $w \sim -1$ ), dragged down by viscous shear forces; the upper one ascends slowly ( $w > 0$ ), due to isopycnals retreating under the effect of buoyancy. It is then reasonable to hypothesize that the buoyancy of the fluid immediately adjacent to the sphere is responsible for the added drag, while the rest of the wake is simply a remnant of the sphere's passage.

Here we rationalize the added drag by a scaling argument based on the buoyancy of a fluid region dragged down by the sphere. For clarity, a dimensional formulation is adopted. Assuming a spherical shell of width  $\delta$ , the volume of this region scales as  $\pi a^2 \delta$ , while its density contrast is  $\Delta \rho = H d\rho/dz$ , where  $H$  is the maximum distance an isopycnal is dragged down. The normalized drag coefficient can then be written as the ratio of this buoyancy force and the homogeneous drag force,

$$C_D^N - 1 \sim \frac{\pi a^2 \delta g \Delta \rho}{C_D^H \frac{1}{2} \rho U^2 \pi a^2} \sim \frac{1}{Fr^2} \frac{1}{C_D^H} \frac{\delta}{a} \frac{H}{a}, \quad (4.3)$$

where  $\delta/a$  and  $H/a$  are still to be determined.

We propose that  $\delta \sim (\nu/N)^{1/2}$ , the natural length scale in a viscous and buoyant flow [3, 5], resulting in  $\delta/a \sim (Fr/Re)^{1/2}$ . This was indeed the scaling of the extent of the fluid shell around the sphere in our numerical data (figure 4-14), for which  $\delta$  was operationally defined as the thickness of the region where  $\Delta\rho$  was  $> 5\%$  of its maximum value, which occurred at the sphere surface. On the other hand, despite considering several possibilities, we were unable to find an *a priori* scaling for  $H$ . At higher  $Re$  ( $\sim O(10^3)$ ),  $H/a \sim Fr$  as a result of a balance between kinetic and potential energy [19], yet this is not applicable in our regime where viscous dissipation is important. Hence, we resorted to an empirical scaling, by computing  $H$  from simulations as the maximum isopycnal deflection immediately upstream of the sphere ( $z = -a$ ). Figure 4-15 shows that  $H/a \sim Fr^{1/2}$ , in line with our earlier observation that isopycnal deflection decreases with increasing stratification. The residual  $Re$  dependence in figure 4-15 is very weak ( $\sim Re^{1/10}$ ) and will be neglected.

With the aforementioned scalings, and using  $C_D^H \sim 1/Re$  (appropriate for small  $Re$ ), equation (4.3) reduces to  $C_D^N - 1 \sim Ri^{1/2}$ . This compares favourably with our result  $C_D^N - 1 \sim Ri^q$ , where  $q = 0.62$  from experiments,  $q = 0.41$  from numerics, for an average of  $q = 0.51$ . These results suggest a new expression for the drag coefficient in a salt-stratified ambient,

$$C_D^S = \left( \frac{12}{Re} + \frac{6}{1 + \sqrt{2Re}} + 0.4 \right) (1 + \alpha Ri^{1/2}), \quad (4.4)$$

where  $\alpha = 1.9$  ( $\alpha = 1.95$  and  $1.91$  in experiments and numerics, respectively). This rationalization of the added drag also applies to the moderate  $Re$  regime, where the dragged-down region scales with the drift volume ( $\sim a^3$ ),  $H/a \sim Fr$  [19], and  $C_D^H \sim Re^0$ ; resulting in  $C_D^N - 1 \sim Fr^{-1}$  which is verified by analysis of the data in Torres *et al.* [43] (Figure 4-16.  $Fr^{-1}$  provides a much better dependence than  $Ri$  in terms on collapsing the data on one single curve in this regime of higher  $Re$ .) and is in agreement with Higginson *et al.* [19].

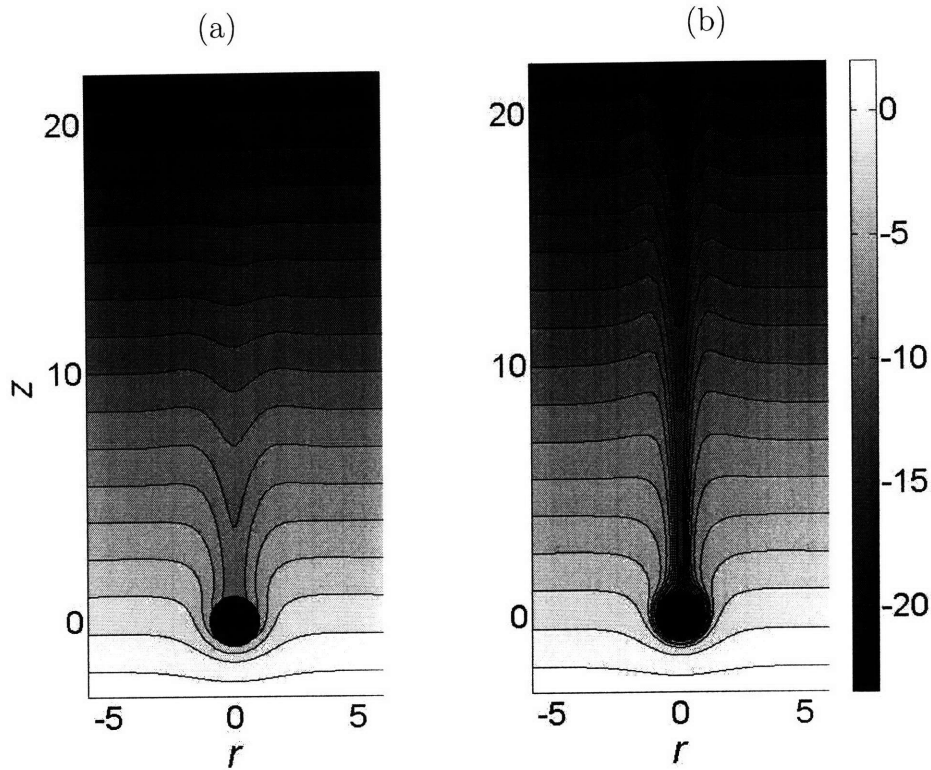


Figure 4-11: Numerical density field  $\rho - \rho(0)$  in the wake of a settling sphere for  $Ri = 0.43$  obtained from (a)  $Re = 0.05$ ,  $Fr = 0.34$  and (b)  $Re = 0.5$ ,  $Fr = 1.08$ . Note the strong difference in the wake structure, except in the region closest to the sphere.

In general, the problem of a sphere settling through a stratified fluid further depends on  $Pr$ . While our study focused on salt-stratifications ( $Pr = 700$ ), the case of a thermal stratification ( $Pr = 7$ ) is also of relevance in aquatic environments. For this case, simulations show a smaller increase in drag due to stratification (figure 4-2) and a weaker dependence on  $Ri$  ( $q = 0.29$ ). This can be rationalized by considering that stronger diffusion more effectively counteracts the accumulation of buoyancy forces by more rapidly smoothing out isopycnal deflections. This is shown in figure 4-17, which compares the wake for  $Pr = 7$ , 100 and 700: isopycnal deflections decrease with  $Pr$  (see also figure 4-15) and the wake becomes shorter and wider (see also figure 4-13).

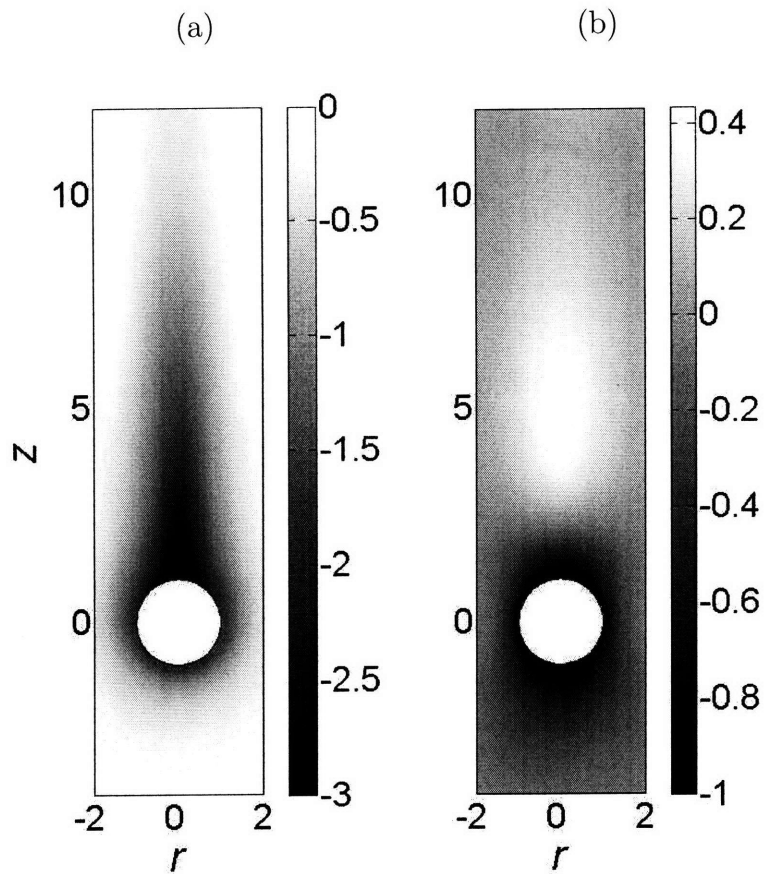


Figure 4-12: (a) Density contrast  $\Delta\rho$  and (b) vertical fluid velocity  $w$  in the wake of a settling sphere for  $Ri = 0.29$  ( $Re = 0.05$ ,  $Fr = 0.42$ ). The long wake (panel a) comprises two distinct regions (panel b): the lower one travels at a speed comparable to that of the sphere ( $w \sim -1$ ).

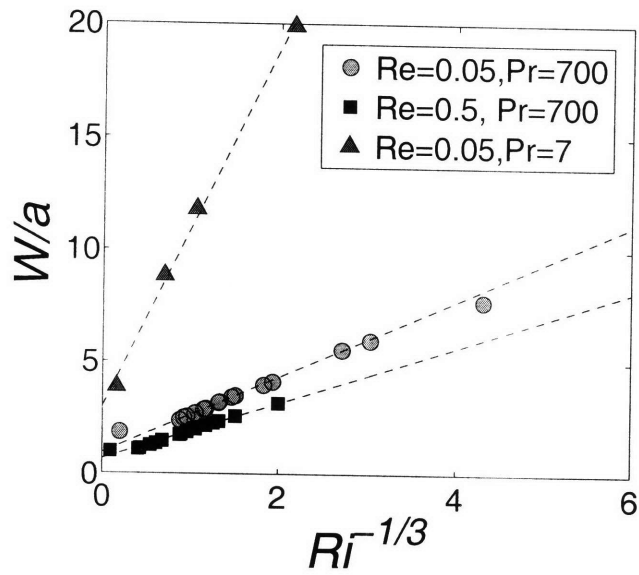


Figure 4-13: The width of the wake  $W$  as a function of  $Ri^{-1/3}$ .

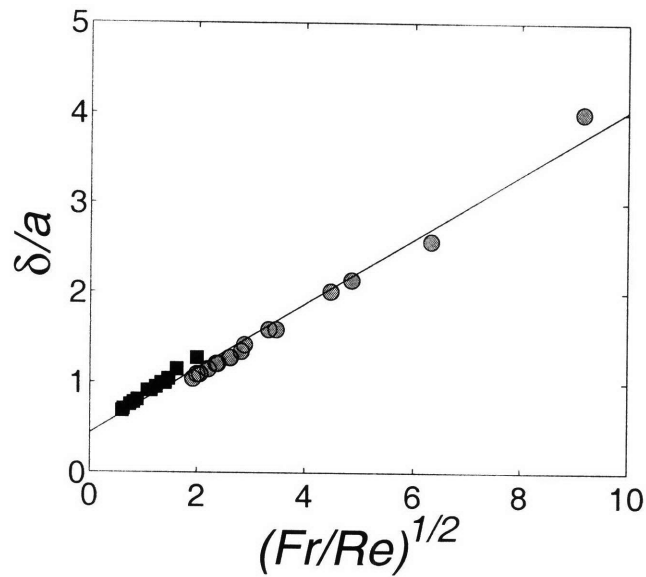


Figure 4-14: The length scale  $\delta$  of the fluid region responsible for the added drag, as a function of  $(Fr/Re)^{1/2}$ .

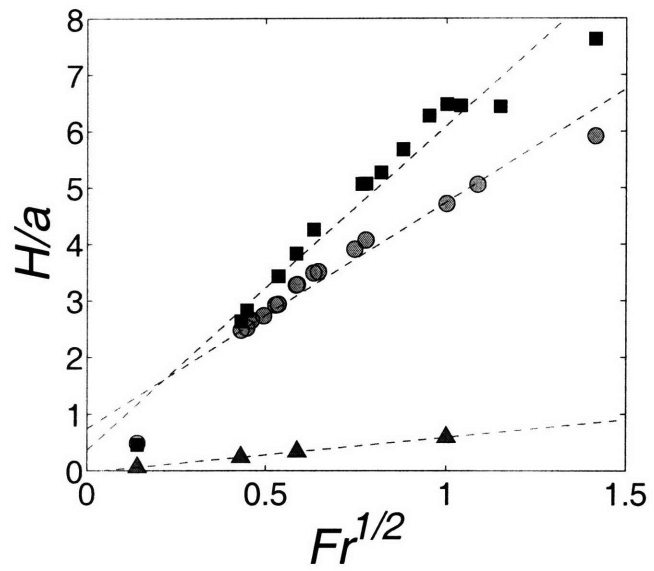


Figure 4-15: The maximum isopycnal deflection  $H$  as a function of  $Fr^{1/2}$ .  $W$ ,  $\delta$  and  $H$  were computed from numerical simulations as described in the text and nondimensionalized by  $a$ .

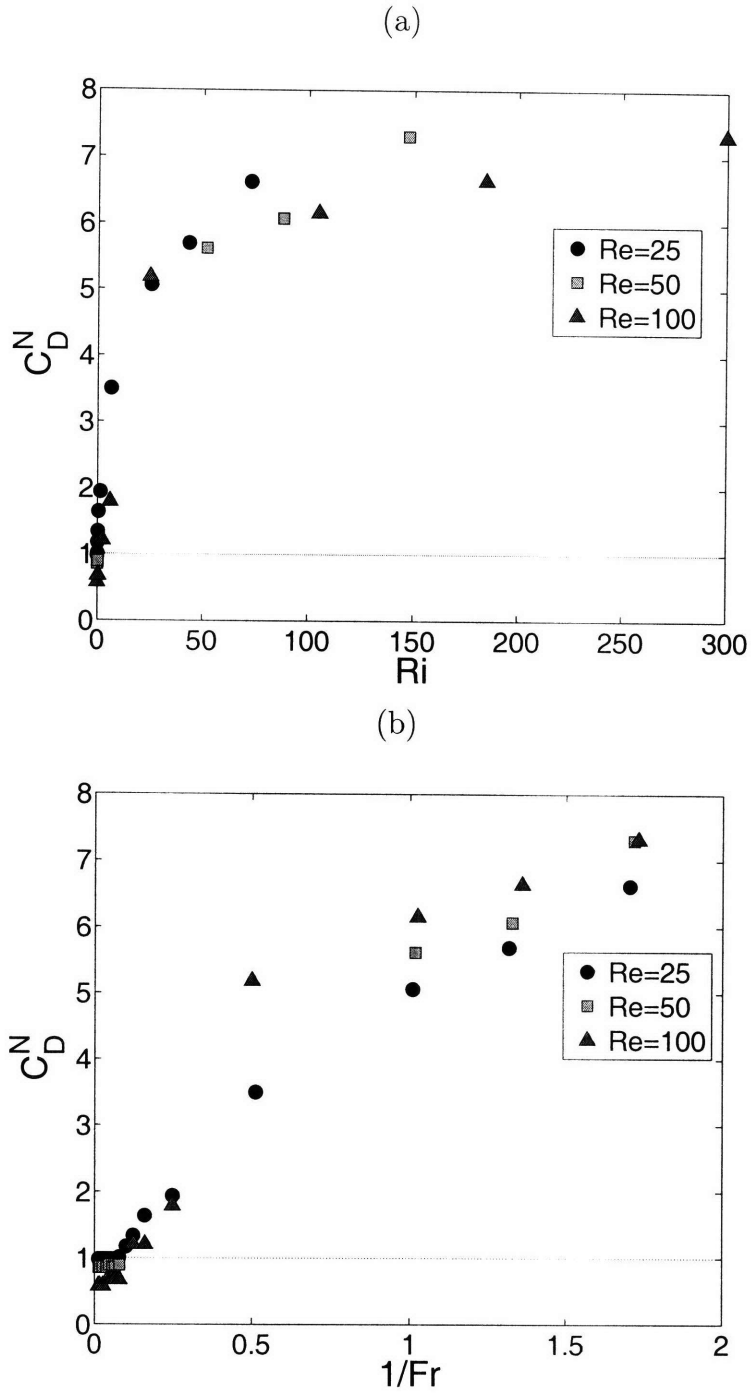


Figure 4-16: (a) The normalized drag coefficient  $C_D^N$  as a function of  $Ri$  for numerical simulations at high  $Re$ . (b) The normalized drag coefficient  $C_D^N$  as a function of  $1/Fr$  for numerical simulations at high  $Re$ . Data were obtained by examining the published data in Torres *et al.* [43] visually.



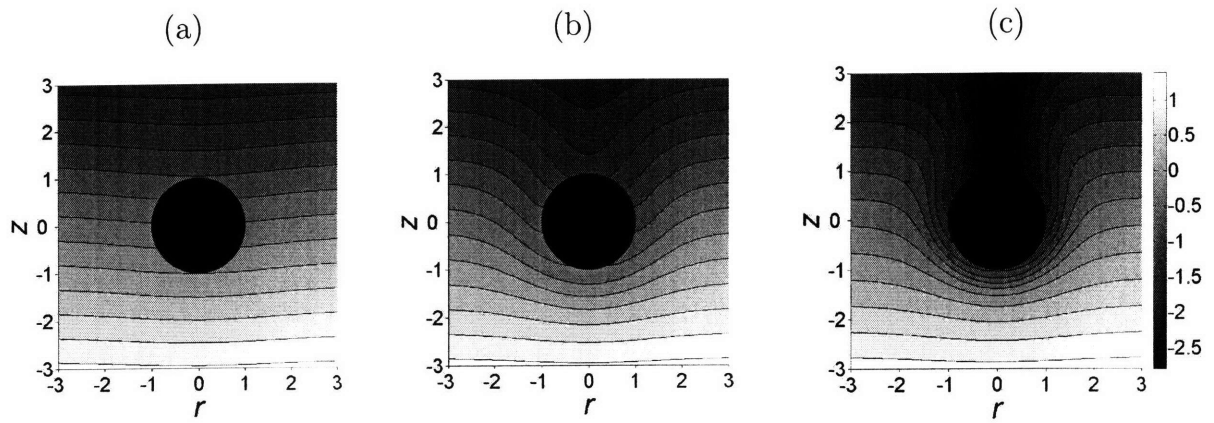


Figure 4-17: Numerical density field  $\rho - \rho(0)$  for (a)  $Pr = 7$ , (b)  $Pr = 100$ , (c)  $Pr = 700$ . In all panels,  $Ri = 1.25$  ( $Re = 0.05$ ,  $Fr = 0.2$ ).



# Chapter 5

## Conclusion

The observed added drag implies that a sphere settles more slowly in a stratified fluid than predicted using homogeneous-fluid formulations. Figure 5-1(a) shows the experimental trajectory of an  $a = 196 \mu\text{m}$  sphere in a stratification with  $N = 1.69 \text{ s}^{-1}$ , compared to its expected trajectory in a homogeneous fluid. The distance traveled over 100 s is roughly half in the stratified case, and is predicted to within 10% by our drag coefficient formulation (4.4). How important is this effect in natural stratified environments? Some of the strongest aquatic stratifications are found in inlets, fjords and river outflows, where freshwater overlying saltier water can result in  $N$  being as large as  $0.2 \text{ s}^{-1}$  [14](figure 2A). While freshwater lakes can be nearly as strongly stratified due to temperature [31, 21], the corresponding Prandtl number is much smaller and the influence of stratification therefore reduced. Heading further out into the ocean, density gradients are generally weaker, reaching maximum values on the order of  $N \sim 0.02 \text{ s}^{-1}$ . The role of salt-stratifications was investigated by plotting the ratio of stratified to homogeneous travel time (figure 5-1(b)); these were found by integrating the settling speed  $U$ , determined numerically from equation (3.3) using the stratified (equation 4.4) and homogeneous (equation 3.2) drag coefficients. This procedure was repeated for a range of particle sizes up to  $a = 2500 \mu\text{m}$  and three values of the density contrast  $\Delta\rho = 1, 5$  and  $20 \text{ kg m}^{-3}$ , representative of biological matter. The effect of stratification increases with particle size, as expected from the  $Ri$  dependence. In the open ocean we predict the increase in settling time due to

stratification is  $< 6\%$ , rising significantly to  $66\%$  for strongly stratified fjords and inlets. This suggests that the effect of stratification on settling time needs to be accounted for in strongly stratified natural water bodies. We expect this effect to be compounded by hindered settling due to particle-particle interactions in particle clouds [6, 4].

We have presented a combined theoretical, experimental and numerical investigation of the fluid mechanics of a sphere settling in a linearly stratified fluid at small Reynolds numbers. To enable a quantitative study of the density field in a stratified fluid for small particles, we have extended the technique of Synthetic Schlieren to the microscale. We have performed the first visualization of the wake structure behind a settling sphere in a stratified fluid at low  $Re$ . This study provides the first experimental evidence of stratification-induced enhanced drag in a continuously stratified fluid at small  $Re$ , further supported by numerical simulations. This parameter regime is particularly important in the ocean, where density interfaces are ubiquitous and a large fraction of the particle size spectrum is composed of sub-millimeter particles with small density contrast with the ambient fluid. The increase in drag is governed by a single dimensionless parameter, the Richardson number, expressing the relative importance of buoyancy and shear forces. The normalized drag coefficient  $C_D^N$  was found to scale like  $1 + 1.9 Ri^{0.51}$ , with a small discrepancy in the exponent ( $\pm 0.1$ ) between numerics and experiments. Microscale Synthetic Schlieren revealed that a particle's signature lingers long after it has passed, producing an extended wake in which density is perturbed. Careful analysis of the flow and density fields showed that only a minor portion of the wake is responsible for the added drag, enabling us to rationalize observations via a scaling argument. The added drag decreases with  $Pr$ , as diffusion increasingly counteracts buoyancy. This effect is relevant to strongly stratified aquatic environments (e.g. inlets and fjords, and to a lesser extent the open ocean and lakes), where it can enhance retention of biological material at density interfaces [26] and colonization of marine snow aggregates by microorganisms [39], ultimately affecting vertical fluxes of matter in biogeochemical cycles.

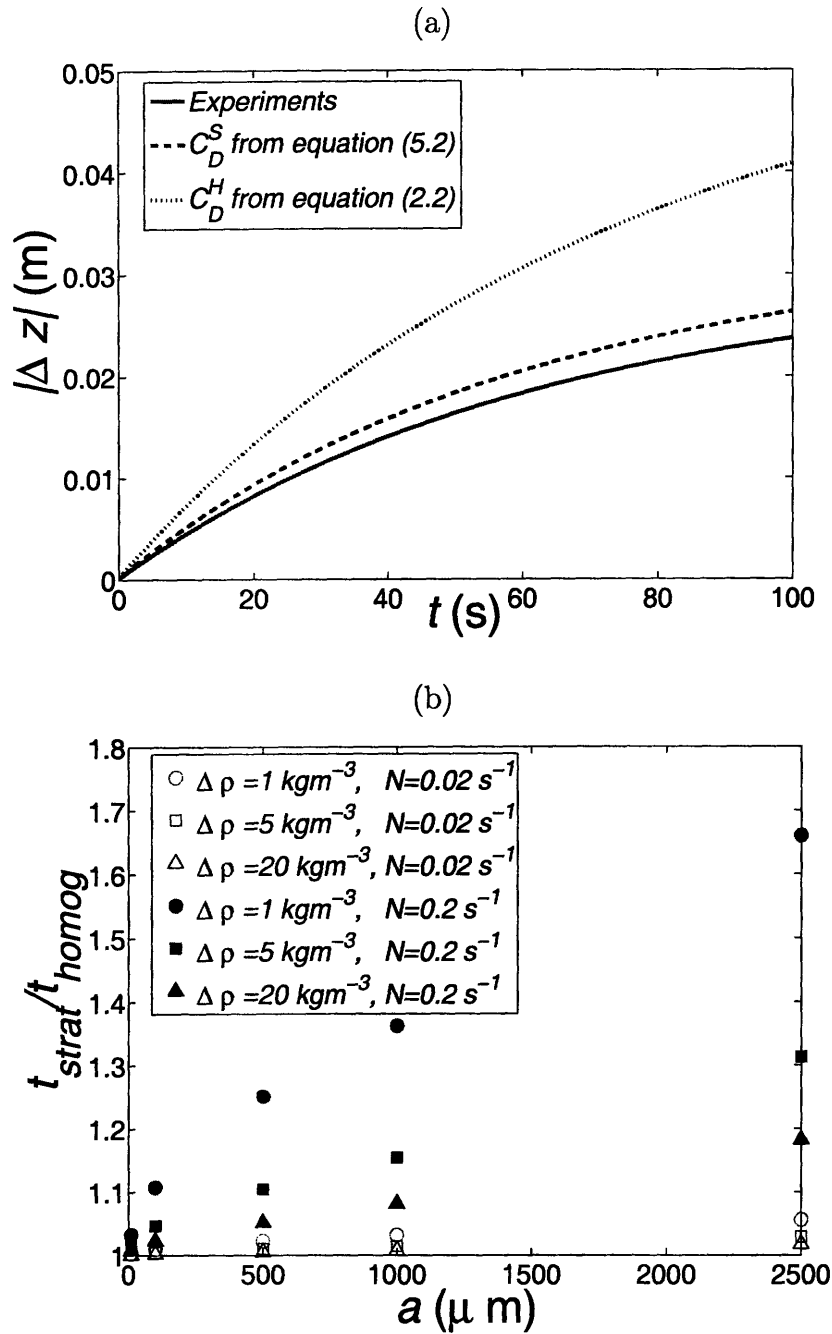


Figure 5-1: (a) Trajectory of an  $a = 196 \mu\text{m}$  sphere settling in stratified fluid with  $N = 1.69 \text{ s}^{-1}$ , determined experimentally (solid line) and predicted using the stratified drag coefficient from equation (4.4) (dashed line). Also shown is the trajectory of the same particle assuming a locally homogeneous drag formulation, equation (3.2) (dotted line). (b) The ratio of travel times computed using a stratified drag coefficient versus a locally homogeneous one, as a function of particle size  $a$ , density contrast  $\Delta\rho$  and stratification  $N$ .

## 5.1 Ideas for future work

Our work also pointed to topics for future investigation. Future work could be directed towards the experimental verification of the normalized drag coefficient  $C_D^N$  at higher  $Re$ , which we postulated scales like  $1/Fr$ . There should then be a transition regime, where the scaling with  $Ri$  shifts to a scaling with  $Fr$ : this is equivalent to a different dependence on  $Re$ , as occurs in a homogeneous fluid. Ultimately, one would want a scaling for  $C_D^N$  spanning a wide range of  $Re$ . Another extension of our work would be to elucidate the dependence of the drag law on Prandtl number. Furthermore, an independent numerical simulation or an extension of the flow visualization technique to visualize the density field immediately adjacent to the sphere, could potentially shed light on the discrepancies in the wake structure between numerical and experimental results. Finally, other interesting avenues of exploration include the role of particle shape and the verification of the proposed drag law (equation 4.4) *in situ* using underwater videography in regions of strong stratification.

# Appendix A

## A mathematical justification of suppression of vertical motion in a stratified fluid

In this appendix we provide a simple scaling argument to show that vertical motion is suppressed in a stratified fluid [52], which is adapted from [27]. Consider an inviscid incompressible, non-diffusive fluid. The equations governing the flow are

$$u_x + v_y + w_z = 0 \tag{A.1}$$

$$u\rho_x + v\rho_y + w\rho_z = 0 \tag{A.2}$$

$$\rho(uu_x + vv_y + ww_z) = -p_x \tag{A.3}$$

$$\rho(uv_x + vv_y + ww_z) = -p_y \tag{A.4}$$

$$\rho(uw_x + vw_y + ww_z) = -p_z - g\rho \tag{A.5}$$

where  $(x, y, z)$  are cartesian coordinates with  $z$  being the vertical direction,  $(u, v, w)$  are fluid velocity components in the direction of  $(x, y, z)$ ,  $p$  is pressure,  $\rho$  is density and  $g$  is acceleration of gravity. The equations can be nondimensionalized by a reference

density  $\rho_o$ , velocity scale  $U$ , pressure scale  $\rho_o U^2$ , and length scale  $L$ , where

$$U = \sqrt{gL} \quad (\text{A.6})$$

and

$$L = \left( \frac{-1}{\rho_o} \frac{d\rho_o}{dz} \right)^{-1} \quad (\text{A.7})$$

where  $d\rho_o/dz$  is the density gradient. Since velocity scale is chosen on dimensional basis alone, it may not represent the actual magnitude and therefore the dimensionless velocity components need not all be  $O(1)$ . The nondimensionalized equations are then written as:

$$u_x + v_y + w_z = 0, \quad (\text{A.8})$$

$$u\rho_x + v\rho_y + w\rho_z = 0, \quad (\text{A.9})$$

$$\rho(uu_x + vv_y + ww_z) = -p_x, \quad (\text{A.10})$$

$$\rho(uw_x + vw_y + ww_z) = -p_y, \quad (\text{A.11})$$

$$\rho(uw_x + vw_y + ww_z) = -p_z - \rho, \quad (\text{A.12})$$

Since  $L$  represents the scale of stratification,  $\rho_z = O(1)$ . Assume  $(u, v, w) \leq O(\epsilon) \ll 1$ . Eliminate  $p$  from equation (A.10) and equation (A.12)

$$\rho_x = \frac{\partial}{\partial z} [\rho(uu_x + vv_y + ww_z)] - \frac{\partial}{\partial x} [\rho(uw_x + vw_y + ww_z)] \quad (\text{A.13})$$

which implies  $\rho_z = O(\epsilon^2)$ . Similarly from equation (A.11) and equation (A.12),  $\rho_y = O(\epsilon^2)$ . Then from equation (A.9),

$$w = O(\epsilon^3) \quad (\text{A.14})$$

which shows that vertical fluid motion is suppressed and the flow is primarily



horizontal. Moreover, equation (A.8) can then be approximated as

$$u_x + v_y = O(\epsilon^3) \tag{A.15}$$

use this in equation A.10

$$\rho(uu_x + vv_y) + O(\epsilon^4) = -p_x \tag{A.16}$$

hence

$$p_x = O(\epsilon^2) \tag{A.17}$$

similarly, from equation (A.10) we can get

$$p_y = O(\epsilon^2) \tag{A.18}$$

Finally from equation (A.12)

$$-p_z - \rho = O(\epsilon^4) \tag{A.19}$$

therefore the pressure is hydrostatic. The scaling argument here shows that, to the leading order, the flow is primarily two dimensional in the horizontal plane.



# Bibliography

- [1] ABAID, N., ADALSTEINSSON, D., AGYAPONG, A. & MCCLAUGHLIN, R.M. 2004 An internal splash: Levitation of falling spheres in a stratified fluid. *Phys. Fluids* **16**, 1567.
- [2] AZAM, F. & LONG, R.A. 2001 Sea snow microcosms. *Nature* **414**, 495–498
- [3] BASAK, S. & SARKAR, S. 2006 Dynamics of a stratified shear layer with horizontal shear. *J. Fluid Mech.* **568**, 19–54.
- [4] BLANCHETTE, F. & BUSH, J.W.M. 2005 Particle concentration evolution and sedimentation-induced instabilities in a stably stratified environment. *Phys. Fluids* **17**, 073302.
- [5] BLANCHETTE, F., PEACOCK, T. & COUSIN, R. 2008 Stability of a stratified fluid with a vertically moving side-wall. *J. Fluid Mech.* **609**, 305–317.
- [6] BUSH, J.W.M., THURBER, B.A. & BLANCHETTE, F. 2003 Particle clouds in homogeneous and stratified environments. *J. Fluid Mech.* **489**, 29–54.
- [7] BURTON, R.A. 1949 A modified schlieren apparatus for large areas of field. *J. Opt. Soc. Amer.* **39**, 907–909
- [8] CLIFT, R., GRACE, J.R. & WEBER, M.E. 1978 *Bubbles, Drops, and Particles*, 380 pp. Academic Press.
- [9] DALZIEL, S.B. 1992 Decay of rotating turbulence: some particle tracking experiments. *Appl. Scien. Res.* **49**, 217–244.

- [10] DALZIEL, S.B., HUGHES, G.O. & SUTHERLAND, B.R. 2000 Whole-field density measurements by 'synthetic schlieren' *Expts Fluids* **28**, 322–335
- [11] DIGIFLOW 2006 [www.damtp.cam.ac.uk/lab/digiflow](http://www.damtp.cam.ac.uk/lab/digiflow).
- [12] DAVIS, R.H. & ACRIVOS, A. 1985 Sedimentation of noncolloidal particles at low reynolds numbers *Ann. Rev. Fluid Mech.* **17**, 91–118
- [13] EAMES, I., GOBBY, D. & DALZIEL, S.B. 2003 Fluid displacement by Stokes flow past a spherical droplet. *J. Fluid Mech.* **485**, 67–85.
- [14] FARMER, D. & ARMI, L. 1999 The generation and trapping of solitary waves over topography. *Science* **283**, 188–190.
- [15] FLYNN, M.R., ONU, K.O. & SUTHERLAND, B.R. 2003 Internal wave excitation by a vertically oscillating sphere *J. Fluid Mech.* **494**, 65–93
- [16] FOFONOFF, P. & MILLARD, R.C. JR 1983 Algorithms for computation of fundamental properties of seawater. *Unesco Tech. Pap. Mar. Sci.* **44**, 53.
- [17] GREENSLADE, M.D. 1994 Strongly stratified airflow over and around mountains. In *Stably Stratified Flows: Flow and Dispersion over Topography, Proc. 4th IMA Conf. on Stably Stratified Flows, University of Surrey, Sept. 1992*, eds. I.P. Castro and N.J. Rockliff, Oxford University Press .
- [18] GREENSLADE, M.D. 2000 Drag on a sphere moving horizontally in a stratified fluid. *J. Fluid Mech.* **418**, 339–350.
- [19] HIGGINSON, R.C., DALZIEL, S.B. & LINDEN, P.F. 2003 The drag on a vertically moving grid of bars in a linearly stratified fluid. *Expts. Fluids* **34**, 678–686.
- [20] KELLOGG, W.N. 1990 Aerosols and climate. In *Interaction of Energy and Climate*, eds. W. Bach, J. Pankrath and J. Williams. Reidel .
- [21] KING, J.R., SHUTER, B.J. & ZIMMERMAN, A.P. 1999 Signals of climate trends and extreme events in the thermal stratification pattern of multibasin Lake Opeongo, Ontario. *Can. J. Fish. Aquat. Sci.* **56**, 847–852.

- [22] KIORBOE, T. & JACKSON, G.A. 2001 Marine snow, organic solute plumes and optimal chemosensory behavior of bacteria. *Limnology and Oceanography* **46**, 1309–1318.
- [23] LARRAZÁBAL, G., TORRES, C.R. & CASTILLO, J. 2003 An efficient and robust algorithm for 2D stratified fluid flow calculations. *Appl. Num. Math.* **47**, 493–502.
- [24] LEAL, L.G. 1980 Particle motions in a viscous fluid. *Ann. Rev. Fluid Mech.* **12**, 435–476.
- [25] LOFQUIST, K.E.B. & PURTELL, L.P. 1984 Drag on a sphere moving horizontally through a stratified liquid. *J. Fluid Mech.* **148**, 271–284.
- [26] MACINTYRE, S., ALLDREDGE, A.L. & GOTSCHALK, C.C. 1995 Accumulation of marine snow at density discontinuities in the water column. *Limnol. Oceanogr.* **40**, 449–468.
- [27] MEI, C.C. Lecture notes of MIT course 2.21 Environmental Fluid Dynamics
- [28] OCHOA, J.L. & Van Woert, M.L. 1977 Flow visualization of boundary layer separation in a stratified fluid. *Unpublished report, Scripps Institution of Oceanography* **28**.
- [29] ONU, K., FLYNN, M.R. & SUTHERLAND, B.R. 2003 Schlieren measurement of axisymmetric internal waves *Expts. Fluids* **35**, 24–31
- [30] OSTER, G. 1965 Density gradients. *Sci. Am.* **213**, 70.
- [31] PATTERSON, J.C., HAMBLIN, P.F. & IMBERGER, J. 1984 Classification and dynamic simulation of the vertical density structure of lakes. *Limnol. Oceanogr.* **29**, 845–861.
- [32] PEACOCK, T., BLANCHETTE, F. & BUSH, J.W.M. 2005 The stratified boycott effect *J. Fluid Mech.* **529**, 33–49
- [33] PEACOCK, T. & TABAEI, A. 2005 Visualization of nonlinear effects in reflecting internal wave beams *Phys. Fluids*, **17**, 061702

- [34] RICHARD, H. & RAFFEL, M. 2001 Principle and applications of the background oriented schlieren (BOS) method *Meas. Sci. Tech.* **12**, 1576–1585
- [35] SCASE, M.M. & DALZIEL, S.B. 2004 Internal wave fields and drag generated by a translating body in a stratified fluid. *J. Fluid Mech.* **498**, 289–313.
- [36] SMITH, R.B. 1979 The influence of mountains on the atmosphere. *Advances in Geophysics*, Vol. 21. New York: Academic Press.
- [37] SMITH, R.B. 1980 Linear theory of stratified hydrostatic flow past an isolated mountain. *Tellus* **32**, 348–364.
- [38] SRDIĆ-MITROVIĆ, A.N., MOHAMED, N.A. & FERNANDO, J.S. 1999 Gravitational settling of particles through density interfaces. *J. Fluid Mech.* **381**, 175–198.
- [39] STOCKER, R., SEYMOUR, J.R., SAMADANI, A., HUNT, D.E. & POLZ, M.F. 2008 Rapid chemotactic response enables marine bacteria to exploit ephemeral microscale nutrient patches. *Proc. Natl. Acad. Sci.* **105**, 4209–4214.
- [40] SUTHERLAND, B.R., DALZIEL, S.B., HUGHES, G.O. & LINDEN, P.F. 1999 Visualisation and measurement of internal waves by ‘synthetic schlieren’. Part I: vertically oscillating cylinder *J. Fluid Mech.* **390**, 93–126
- [41] TENNER, A.R. & GEBHART, B. 1971 Laminar and axisymmetric vertical jets in a stably stratified environment. *Int. J. Heat Mass Transfer* **14**, 2051–2062.
- [42] TOPLER, A. 1864 Beobachtungen nach einer neuen optischen Methode. Max Cohen u. Sohn, Bonn.
- [43] TORRES, C.R., HANAZAKI, H., OCHOA, J., CASTILLO, J. & Van Woert, M. 2000 Flow past a sphere moving vertically in a stratified diffusive fluid. *J. Fluid Mech.* **417**, 211–236.
- [44] TRITTON, D.J. 1988 *Physical Fluid Mechanics*, 2nd ed, 519 pp. Oxford University Press.

- [45] TURCO, R.P., TOON, O.B., ACKERMAN, T.P., POLLACK, J.B. & SAGAN, C. 1990 Climate and smoke: An appraisal of nuclear winter. *Science* **247**, 166–176.
- [46] VENKATAKRISHNAN, L. & MEIER, GEAL 2004 Density measurements using the Background Oriented Schlieren technique *Expt. Fluids* **37**, 237–247
- [47] VOSPER, S.B., CASTRO, I.P., SNYDER, W.H. & MOBBS, S.D. 1999 Experimental studies of strongly stratified flow past three-dimensional orography. *J. Fluid Mech.* **390**, 223–249.
- [48] WARREN, F.W.G. 1960 Wave resistance to vertical motion in a stratified fluid. *J. Fluid Mech.* **7**, 209–229.
- [49] WEYL, F.J. 1954 Analysis of optical methods. In Ladenburg R.W. (ed) *Physical measurements in gas dynamics and combustion*. Princeton University Press, Princeton, New Jersey, 3–25
- [50] WHITE, F.M. 2005 *Viscous Fluid Flow*, 3rd ed., 640 pp. McGraw-Hill.
- [51] YICK, K.Y., STOCKER, R. & PEACOCK, T. 2006 Microscale synthetic schlieren. *Expts. Fluids* **42**, 41–48.
- [52] YIH, C.S. 1980 *Stratified Flows*, 2nd ed., 458 pp. Academic Press.
- [53] ZVIRIN, Y. & CHADWICK, R.S. 1974 Settling of an axially symmetric body in a viscous stratified fluid. *Int. J. Multiph. Flow* **1**, 743–752.